UCRL-10718

Cy 4

University of California

Ernest O. Lawrence Radiation Laboratory

EFFECTS OF THE SINGLE PION EXCHANGE IN THE REACTION $p+p \rightarrow n+p+\pi^+$

Berkeley, California

DISCLAIMER

This document was prepared as an account of work sponsored by the United States Government. While this document is believed to contain correct information, neither the United States Government nor any agency thereof, nor the Regents of the University of California, nor any of their employees, makes any warranty, express or implied, or assumes any legal responsibility for the accuracy, completeness, or usefulness of any information, apparatus, product, or process disclosed, or represents that its use would not infringe privately owned rights. Reference herein to any specific commercial product, process, or service by its trade name, trademark, manufacturer, or otherwise, does not necessarily constitute or imply its endorsement, recommendation, or favoring by the United States Government or any agency thereof, or the Regents of the University of California. The views and opinions of authors expressed herein do not necessarily state or reflect those of the United States Government or any agency thereof or the Regents of the University of California.

UCRL-10718
UC Physics
TID-4500 (19th Ed.)

UNIVERSITY OF CALIFORNIA
Lawrence Radiation Laboratory
Berkeley, California

Contract No. W-7405-eng-48

EFFECTS OF THE SINGLE PION EXCHANGE IN THE REACTION $p + p \rightarrow n + p\ \pi^+$

Joseph T. Lach

(Ph. D. Thesis)

March 11, 1963

Printed in USA. Price $2.25. Available from the
Office of Technical Services
U. S. Department of Commerce
Washington 25, D.C.

EFFECTS OF THE SINGLE PION EXCHANGE IN THE REACTION $p + p \rightarrow n + p + \pi^+$

Contents

Abstract v

I. Introduction 1

II. Design Considerations 9

III. Description of Apparatus

A. Detector Geometry 14

B. Neutral Pion Discrimination 17

C. Incident Beam 17

D. Electronics 23

IV. Raw Data 32

V. Systematic Corrections

A. Sources and Description 36

1. Neutron Detection Efficiency 36

2. Kinematical Fitting Program 36

3. Geometrical Corrections 38

4. Overlap and Range Corrections 39

5. Scattering Corrections 39

B. The Monte Carlo Comparison — DRYLAB 40

C. Efficiency and Resolution of Detectors

1. Integrated Efficiencies 54

2. Resolutions 56

3. Scattering Corrections Applied 61

VI. Results, Discussion, and Conclusions

A. Primary Data 63

B. Analysis of the Data in W^2 63

C. Analysis of the Data in P^2 72

VII. Conclusions 83

Acknowledgments 84

Appendix A. Summary Of Three-Body Kinematics 85

Appendix B. Calibration of Neutron Detectors 95

Appendix C. A Survey of Positive Pion-Proton Scattering Distributions 96

Footnotes and References 102

EFFECTS OF THE SINGLE PION EXCHANGE IN THE REACTION $p + p \rightarrow n + p + \pi^+$

Joseph T. Lach

Lawrence Radiation Laboratory
University of California
Berkeley, California

March 11, 1963

ABSTRACT

The distribution of neutrons in energy and angle from the reaction $p + p \rightarrow n + p + \pi^+$ at an incident proton momentum of 2.5 BeV/c is studied. The coordinates of the three final-state particles are measured by an array of plastic scintillation counters, the energy of the recoil neutron being determined through its flight time. The range of measured neutron angles is limited to 4 to 60 deg, and the range of recoil momentum is from approximately 150 to 330 MeV/c. Data is recorded on magnetic tape in a format directly acceptable to an IBM 7090 computer where sorting and kinematical fitting is done.

A Monte Carlo computation is made in which the effects of the complex resolution functions of the apparatus and the fitting code are investigated and used to compute the overall efficiency and resolution of the apparatus. Because of geometrical limitations of the angular region in which the final state pion and proton could be detected, and our inability to distinguish between them in 18% of the events, the analysis is limited to a region of θ^*, the pion-proton scattering angle, bounded by $-0.5 < \cos(\theta^*) < +0.5$. Comparisons are made with predictions of the one-pion exchange model. A Chew-Low extrapolation is performed and deviations from a linear extrapolation are found. The peripheral model predictions of Selleri agree well with the observed position and reasonably well with the observed shape of the 3/2, 3/2 resonance if an integration is made over momentum transfer. The cross section, as a function of momentum transfer, deviates from the predicted behavior.

I. INTRODUCTION

With his postulate of the meson in 1935, Yukawa[1] laid the framework for later attempts to understand the strong interactions in terms of the exchange of finite-mass particles; with the subsequent discovery of the pi meson and the development of quantum field theory, it was hoped that a satisfactory quantitative formulation of the theory of strong interactions could be achieved. Although the meson field theory of nuclear forces has met with some limited successes, such as in the use of the static model by Chew and Low[2] in describing the low energy behavior of the pion-nucleon interaction, quantitative calculations have proven very difficult to make, and their agreement with experimental results has been capricious. These difficulties appear to indicate that nuclear forces cannot be accounted for by a single pion exchange; the role of multiple pion exchanges and even more complicated processes seems to be significant. Although these complications appear formidable, it was felt that there may be conditions under which the simple picture of a single pion exchange is valid; that in these cases, calculations made with this model would give results which would agree with experiments. With this conjecture in mind, we undertook the experiment described in this and two related papers, 4, 5.

Chew and Low,[3] using the single-pion exchange model, were the first to make explicit the connection between production reactions of the form

$$M_1 + M_2 \rightarrow M_3 + M_1 + \mu ,$$

and the elastic scattering reaction

$$M_1 + \mu \rightarrow M_1 + \mu .$$

Here, and in the subsequent sections, the notation of Chew and Low[3] will be slightly modified so that the Latin letter M will always refer to a nucleon and the Greek letter μ will refer to a meson. Appendix A is

a summary of the notation and useful kinematical relations. In our notation M_1 is the mass of the projectile particle, M_2 is the mass of the target particle which is at rest in the laboratory. In this model, the target particle may be considered as virtually composed of a particle of mass M_3, whose role is considered that of a spectator to the reaction, and a lighter particle of mass μ. In the reaction, enough energy is transferred to the target to liberate its constituents. Chew and Low conjecture that from a knowledge of the above production process, one can deduce the behavior of the elastic scattering reaction.

The experiment to be described was one of three done, all using the same apparatus, to investigate such reactions. This paper will concern itself with the reaction

$$p + p \rightarrow n + p + \pi^+$$

where the elastic process

$$\pi^+ + p \rightarrow \pi^+ + p$$

is well known experimentally. The reactions

$$\pi^- + p \rightarrow n + \pi^- + \pi^+$$

and

$$\pi^+ + p \rightarrow n + \pi^+ + \pi^+$$

were also investigated;[4, 5] here, the associated elastic process of pion-pion scattering is inaccessible to direct experimental measurement. We hope in each of these three inelastic processes to find the dominance of the <u>same</u> single pion exchange. Thus, if we could successfully infer the known pion-proton cross section from a knowledge of the associated inelastic process this inference would lend stature to the inference of the totally unknown pion-pion cross section from its associated inelastic process.

For Chew and Low,[3] the essential assumptions are the existence of poles in the scattering amplitude and the dominance of these poles in determining the interaction in their neighborhood. For our production process, where μ represents the pion mass, the position of the single pion pole due to the diagram shown in Fig. 1, can be expressed as a function of Δ^2, the square of the difference of the four-momentum of the target (M_1) and the spectator particle (M_3). The production process in Fig. 1 will then manifest itself as a pole at $\Delta^2 = -\mu^2$, and should dominate the behavior of the amplitude in this neighborhood. One notices, however, that this pole is not in the physical region, and hence we are unable to make measurements in its immediate neighborhood, but must be content to make our measurements in the physically accessible region and extrapolate their value to the pole. Chew and Low[3] give the form of this extrapolation in terms of the more convenient variable P^2 defined as

$$P^2 = 2\, M_3\, T_{3L}$$

which in terms of Δ^2 is

$$P^2 = \frac{M_3}{M_1}\left[\Delta^2 + (M_1 - M_3)^2\right].$$

In the reaction under study, P^2 is approximately equal to Δ^2; it reflects the singularity in Δ^2 as a pole at a value, ${P_0}^2$, given by

$${P_0}^2 = \frac{M_3}{M_1}\left[-\mu^2 + (M_1 - M_3)^2\right].$$

Because ${P_0}^2$ differs from the charged pion mass squared, μ^2, by less than 1.3%, we conform with general usage and approximate it by μ^2. From these relations one sees that P^2 is an invariant, given in the nonrelativistic approximation by just the square of the neutron recoil momentum in the laboratory system. The value of P^2 at the pole, $-\mu^2$, corresponds to a neutron energy of about -10 MeV.

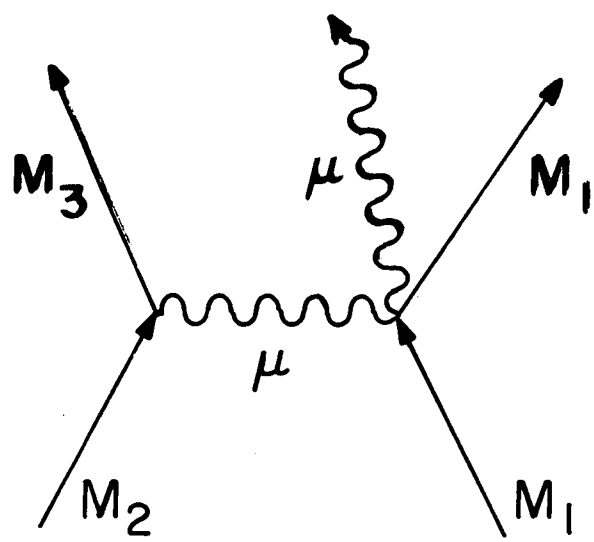

MU-30224

Fig. 1. Diagram of the single pion exchange in the reaction

$$M_1 + M_2 \rightarrow M_1 + M_3 + \mu ,$$

where for the specific reaction under study, M_1 and M_2 refer to a proton, M_3 to a neutron, and μ to the positive pion. Chew and Low assume that only this diagram contributes to the reaction at low momentum transfer.[3]

The extrapolation function, F, that we are required to construct is given by[3]

$$F(P^2, W^2) = 2\pi \left(\frac{M_1}{M_3}\right)^2 \frac{q_{1L}^2 (P^2 + \mu^2)^2}{f^2 R(W)} \frac{\partial^2 \sigma}{\partial P^2 \partial W^2}, \qquad \text{(I-1)}$$

where

$$R(W) = \frac{1}{2} \sqrt{W^4 - 2 W^2 (M_1^2 + \mu^2) + (M_1^2 - \mu^2)^2} .$$

In our case, f^2 is the charged pion-nucleon coupling constant equal to 0.16, and W^2 is an invariant equal to the total energy of the two non-spectator particles measured in their own center-of-mass system. W^2 is given by

$$W^2 = (w_{IL} + M_1 - w_{3L})^2 - (q_{IL}^2 - 2 q_{IL} q_{3L} \cos\theta_{3L} + q_{3L}^2)$$

where w_{IL} = total laboratory energy of the incident particle, M_1 (in this case a proton),

q_{IL} = laboratory momentum of the incident particle,

w_{3L} = total laboratory energy of the spectator particle, M_3 (in this case a neutron),

q_{3L} = laboratory momentum of the spectator particle,

and

θ_{3L} = laboratory polar angle of the spectator particle,

$\frac{\partial^2 \sigma}{\partial P^2 \partial W^2}$ = cross section to be measured per P^2 and per W^2.

Appendix A and Fig. 2 present a systematic description of useful three-body kinematical relations and the notation used in this paper.

If one measures $F(P^2, W^2)$ at a fixed W^2 as a function of P^2 then Chew and Low claim:

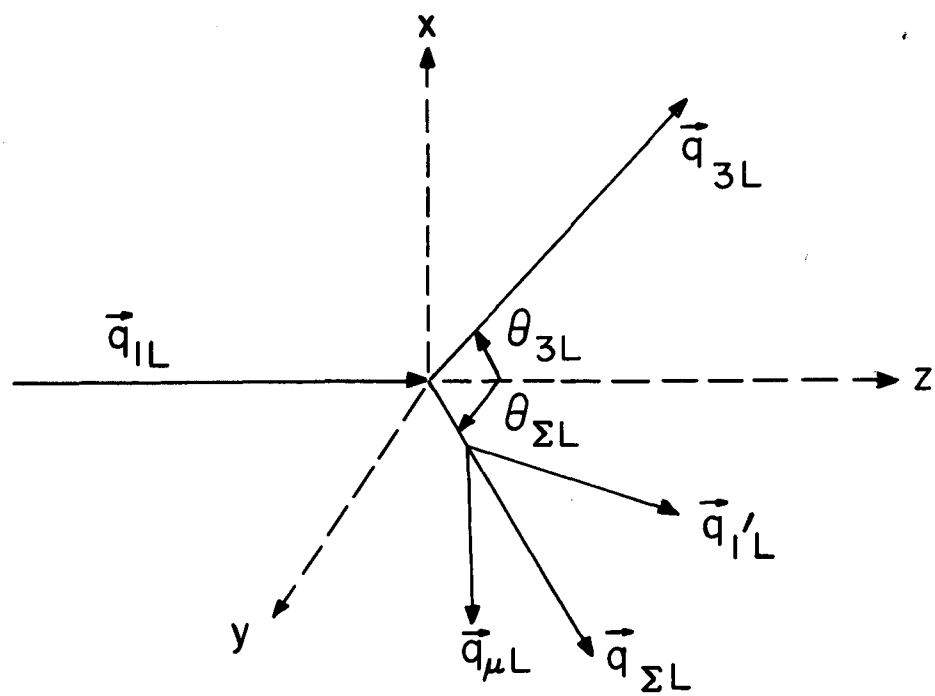

MU-30225

Fig. 2. Kinematics diagram in the laboratory system for the general reaction

$$M_1 + M_2 \rightarrow M_1 + M_3 + \mu,$$

where $\vec{q}_{IL}$ = momentum of incident particle of mass M_I, $\vec{q}_{I'L}$ = momentum of final-state particle of mass M_I, $\vec{q}_{3L}$ = momentum of spectator particle of mass M_3, $\vec{q}_{\mu L}$ = momentum of exchanged meson of mass μ, and $\vec{q}_{\Sigma L}$ = momentum of fictitious particle of mass M_Σ. Since M_Σ is equal to the total energy of the two nonspectator particles measured in their mutual center-of-mass system, this allows us to treat this three-body final-state problem in terms of a two-body final-state problem in which one of the particles of mass M decays into two others of mass M_1 and μ. The quantities θ refer to the polar angles of the above momentum vectors. The subscript L will always refer to the laboratory system.

$$\lim_{P^2 \to -\mu^2} F(P^2, W^2) \to -\sigma(W) \tag{I-2}$$

where $\sigma(W)$ is the total cross section for the scattering of (in our case) free positive pions by free protons at a total center-of-mass energy given by W. Chew and Low also claim that an analogous extrapolation will work for the differential cross section. The measurement of the double distribution, $\frac{\partial^2\sigma}{\partial P^2 \partial W^2}$, and the construction of the function $F(P^2, W^2)$, which we use to test this extrapolation procedure, constitute the primary aims of our experiment.

Selleri[26] assumes that Eq. (I-2) holds not only in the limit of $P^2 \to -\mu^2$, but for all P^2. Then the cross section, $\sigma(W)$, can be inserted into Eq. (I-1) to give an expression for $\frac{\partial^2\sigma}{\partial P^2 \partial W^2}$ which can be directly compared with the measured distribution of the three final-state particles. Selleri's expression was published as an integral:

$$\frac{d\sigma}{dT_{3L}} = \frac{4f^2 M}{\pi q_{IL}^2 \mu^2} \int_W W\, R(W)\, \sigma(W)\, [a(T_{3L}) + b(T_{3L}, W) + c(T_{3L}, W)]\, dW,$$

where

$$a(T_{3L}) = \frac{\Delta_2^2}{(\Delta_2^2 + \mu^2)^2}, \tag{I-3}$$

$$b(T_{3L}, W) = \frac{\Delta_1^2}{(\Delta_1^2 + \mu^2)^2}$$

$$c(T_{3L}, W) = \frac{\phi}{(\Delta_1^2 + \mu^2)(\Delta_2^2 + \mu^2)}$$

and we have

$$\phi = (W - M)\,[(E_{p'_2} + M)\,(E_{p'_1} + M)]^{1/2} \cos\theta_i$$

$$+ (W + M)\,[(E_{p'_2} - M)\,(E_{p'_1} - M)]^{1/2}\,\frac{3\cos^2\theta_i - 1}{2}\,.$$

The quantities $E_{p'_1}$, $E_{p'_2}$, and θ_i are the energies of the initial protons and the angle between their directions, all measured in the center-of-mass system of the final-state pion and proton; Δ_1^2 is the square of the four-momentum transfer from projectile to nonspectator proton, and Δ_2^2 is the square of the four-momentum transfer from the target proton to spectator neutron and is identical to Δ^2 as defined earlier in this section. Selleri has assumed equal masses, M, for proton and neutron. The coupling constant, f^2, as stated in this formula, is taken as 0.08. All other notation has been defined earlier or is described in Appendix A. We may rewrite Eq. (I-3) to put it in a more convenient form for comparison with our data:

$$\frac{\partial^2\sigma}{\partial P^2 \partial W^2} = \frac{f^2}{\pi q_{1L}^2 \mu^2}\, R(W)\,\sigma(W)\,[a(P^2) + b(P^2, W) + c(P^2, W)] \qquad \text{(I-4)}$$

where the relation between P^2 and T_{3L} has been noted.

Note that the term $b(P^2, W)$ arises because the expression must be properly symmetrized to account for the identity of the initial particles. The term $c(P^2, W)$ is merely an interference term arising from $a(P^2)$ and $b(P^2, W)$. In the approximation of $b(P^2, W)$ and $c(P^2, W)$ becoming very small — and they will be small compared to $a(P^2)$ in the range of P^2 we will be concerned with — the above reduces to the expression of Chew and Low (Eq. I-1 but without the limit). This will be referred to as the peripheral model during the rest of the paper.

II. DESIGN CONSIDERATIONS

The most impressive feature of the positive pion-proton elastic cross section when viewed as a function of incident-pion laboratory energy is the large resonance at about 195 MeV. The parameters of this experiment were chosen so that the extrapolated cross sections would be in the region of this resonance. Let us now consider what requirements the position of the pion-proton resonance and the Chew-Low extrapolation scheme imposed on the experiment.

First, a measurement of the neutron energy distribution at small Δ^2 must be made. Hence the neutron energy distribution in our reaction must be measured for as low a range of neutron energies as possible. Blocks of plastic scintillator 15 cm thick were chosen as a suitable detector; the energy of the neutron being determined by its flight time. Of course, the larger the distance over which the timing measurement is made, the more accurate the neutron-energy measurement becomes; however, considerations as to the overall size of the apparatus limited this distance to about 5 ft. The most energetic neutron whose energy could be determined in this manner was about 50 MeV, this limit being set by the accuracy with which timing measurements can be made at this energy. The lower limit to the detectable neutron spectrum is set by the properties of the scintillation material itself. Plastic scintillation material is basically polystyrene, (CH), which although not directly sensitive to neutrons, is sensitive to the recoil protons resulting from the neutrons which scatter as a result of the hydrogen in the plastic. This, combined with inelastic processes involving the carbon, gives rise to scintillation light which is then recorded by the photomultiplier. With low energy neutrons, the amount of light released in these processes becomes very small and the resulting phototube pulses reflect this by a large time "jitter" of their output pulses, making accurate timing measurements very difficult. This imposes a lower limit to the energy measurement of about 5 MeV. From the neutron-proton and neutron-carbon cross sections, it was estimated that the counting efficiency of the scintillator would average about 25% in this 5- to 50-MeV energy interval. The efficiency at a given neutron

energy is very difficult to compute and a direct calibration of the detection efficiency as a function of neutron energy was made later.

Second, to compute W^2 we must also measure the neutron angle. Since the kinematics of the reaction require that the neutrons always go forward in the laboratory system, we contain almost all of them if our neutron counters subtend a forward half-angle of 60 deg. Since we have fixed our neutron energy range, and since we also require our W^2 range to bracket the resonance, we have determined our incident momentum to be around 2.5 BeV/c. Figure 3 describes some of these pertinent kinematics.

Third, the detection system must be able to discriminate among other inelastic processes which also occur at this momentum. For example:

$$
\begin{aligned}
p + p &\rightarrow p + p + \pi^0 \\
&\rightarrow p + n + \pi^+ + \pi^0 \\
&\rightarrow p + p + \pi^- + \pi^+ \\
&\rightarrow \text{higher pion multiplicity processes.}
\end{aligned}
$$

Although the double distribution, $\frac{\partial^2 \sigma}{\partial P^2 \partial W^2}$, can be completely determined from a measurement of only the neutron energy and angle distribution, in order to discriminate against reactions of the above types we decided to measure the coordinates of the two nonspectator particles at the same time. Thus seven quantities were measured; the neutron energy, and the polar and azimuthal coordinates of all three final-state particles. Conservations of energy and momentum state:

$$
\begin{aligned}
q_{1L} &= q_{1'L}\cos(\theta_{1'L}) + q_{3L}\cos(\theta_{3L}) + q_{\mu L}\cos\theta_{\mu L}\,, \\
0 &= q_{1'L}\sin(\theta_{1'L})\cos(\theta_{1'L}) + q_{3L}\sin(\theta_{3L})\cos(\theta_{3L}) + q_{\mu L}\sin(\theta_{\mu L})\cos(\theta_{\mu L}), \\
0 &= q_{1'L}\sin(\theta_{1'L})\sin(\theta_{1'L}) + q_{3L}\sin(\theta_{3L})\sin(\theta_{3L}) + q_{\mu L}\sin(\theta_{\mu L})\sin(\theta_{\mu L}),
\end{aligned}
$$

and

$$
W_{IL} + M_3 = W_{1'L} + W_{3L} + W_{\mu L}\,, \qquad \text{(II-1)}
$$

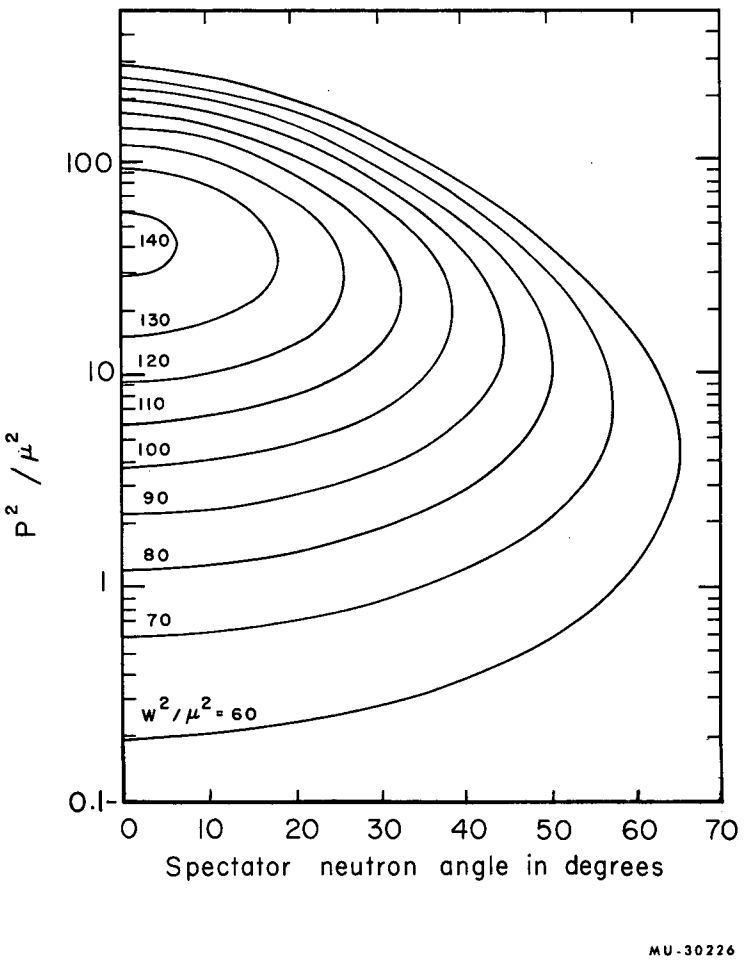

Fig. 3. Accessible region of W^2 in the reaction $p + p \rightarrow n + p + \pi^+$ for an incident proton momentum of 2.5 BeV/c.

where θ is used to refer to the polar angles, ϕ refers to the azimuthal angles of the final-state particles measured in the laboratory system, W is used to represent the total energy of the particle, and M_2 refers to the rest mass of the target particle. Appendix A is a more complete description of the kinematical notation. The three final-state particles can be specified by nine parameters; two angular coordinates and the magnitude of the momentum vector of each particle. Since there are four equations of constraint, a measurement of only five of these nine quantities should determine the entire kinematics. Hence, these measurements will overdetermine the system by two parameters. By demanding that all of our events be consistent with these four equations and the resolution of our geometrical and timing measurements, one imposes powerful criteria for rejecting spurious events.

Although many multiple-pion production events could be discriminated against by the above considerations, the finite resolving power of the system engendered fear that processes involving an additional undetected neutral pion might provide a serious background. These neutral pions could only be detected through the electron-positron pairs produced in the plastic scintillator by the gamma rays resulting from their decay. Since plastic scintillator is essentially a (CH) polymer,[6] it has a relatively long gamma conversion length and hence a low efficiency for detecting gamma radiation. If at least one of the gamma rays resulting from the neutral pion decay could be observed with a high probability, the event could be rejected because it would have more than three observed final-state particles. Without a serious attenuation of the fast charged particles, a thin covering of lead could be applied to all the counters to greatly increase this γ-ray conversion efficiency and alleviate this problem. Such a covering was applied and will be described in more detail in the next section.

Finally, it was realized that in order to achieve the angular resolution necessary to identify the final state particles, a large number of counters would be necessary. The final apparatus consisted of 102 counters, excluding those used to define the incident beam. Recording the data from each of these counters by conventional means such as

scalars was obviously out of the question. Other conventional means such a photographing the outputs of these counters displayed on the face of an oscilloscope seemed unfeasible since the detailed scanning and sorting of the many false events on the film would prove extremely tedious and prohibitively time consuming. Also, with such a system, because of the problems of rapid film transport, only a few possibly good events could be recorded during each Bevatron beam pulse. Consequently, it was decided to record all events in a specially designed high-speed magnetic-core storage unit which would then at periodic intervals transfer its contents to magnetic tape. The analysis and sorting of events would be from this tape by means of a high-speed digital computer.

III. DESCRIPTION OF APPARATUS

A. Detector Geometry

Eighty-four plastic scintillation counters composed the neutron detector. The plastic scintillator in these counters consisted of approximately 97% polystyrene (CH), 3% terphenyl, and 0.03% tetraphenyl butadiene. These counters took the form of trapazoidal prisms set to fit on a section of the surface of a 160-cm radius sphere at whose center was a liquid hydrogen target (Fig. 4). The liquid hydrogen container was a hemispheric Mylar flask 10 cm in radius, the flat side facing the incident beam. The outer vacuum jacket had a Mylar window facing the beam and a 1/16-in.-thick aluminum dome on the other side. Looking outward from the target at the counter array, one would see the elements grouped in a series of seven concentric rings, each ring subtending a polar angular interval of 8 deg. In turn, each ring was divided azimuthally into twelve portions, each portion subtending 30 deg. The entire counter array took the form of an azimuthally symmetric dish covering a region of 4 to 60 deg in polar angle. Light from each of the 15-cm-thick scintillator blocks was channeled by aluminum reflectors into a RCA 6810A photomultiplier for the smaller blocks of the inner three rings or a RCA 7046 photomultiplier for the larger blocks of the outer four rings. Figure 5 is a photograph of the neutron detector array. The total weight of the plastic scintillator was about 1-1/2 tons.

Although the kinematics of the reaction forced the final-state nucleons to go forward in the laboratory system, there was no such restriction for the pions. In order to catch most of the pions a set of thin (1.0 cm) scintillation counters covered the region from 60 to 147 deg in polar angle (Fig. 4). These eighteen counters were overlapped in such a way as to give a resolution of 30 deg in azimuthal angle and divided this polar angular region into four zones ranging in width from 16 deg for the forward zone to 37 deg for the backward zone.

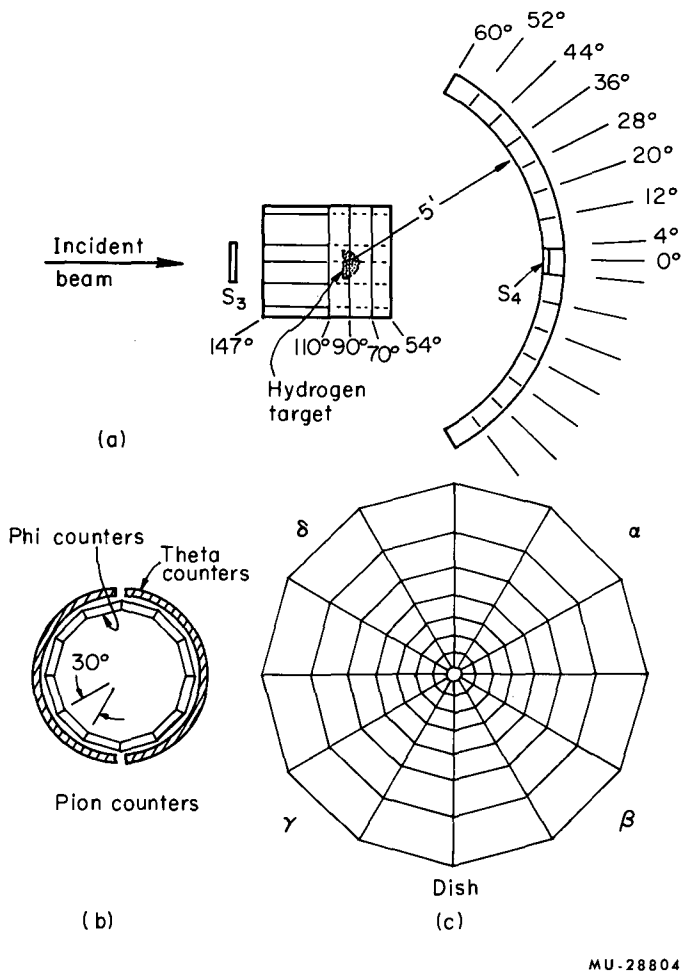

Fig. 4. Geometric arrangement of counters. The side view is shown in (a). Front views of the pion counters and the neutron counters are shown separately in (b) and (c). (View as seen looking along the incident beam.)

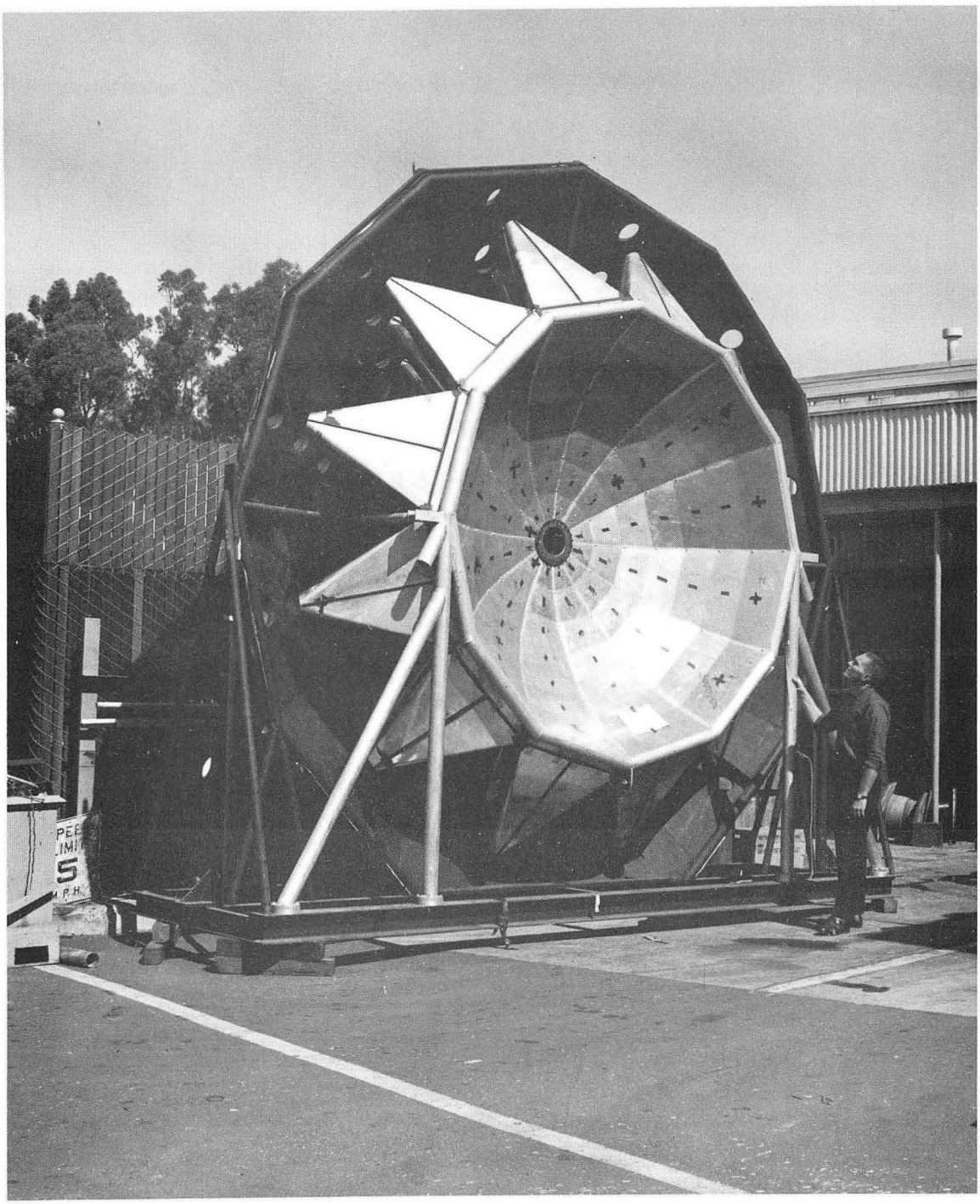

ZN-3412

Fig. 5. Photograph of neutron detector array.

B. Neutral Pion Discrimination

In order to detect gamma rays from the decay of neutral pions, the entire counter array was covered with 0.6 cm of lead sheeting. Assuming that the gamma rays are produced isotropically in the laboratory system, one can calculate the efficiency for detecting those resulting from neutral pion decay. For this calculation, the counter array was divided into three regions, this differentiation being based on the amount of γ-ray conversion material contained in each region. From a knowledge of the radiation lengths in these materials[6] and the relation between the radiation length (l_r) and the γ-ray conversion length[7]

$$l_c = \frac{9}{7} l_r ,$$

one can compute the γ-ray detection efficiency in each of these regions. These are shown in Table I. Summing over all regions, we find the probability of detecting a single gamma ray to be 76%. Hence the probability for detecting at least one of the two γ rays resulting from the pion decay is 94%. Since, in the laboratory system, the interaction will favor forward γ-ray production where the detection efficiency is greatest, this pion discrimination probability should be considered a lower limit.

C. Incident Beam

Since the same magnet system was to be used to investigate pion-production processes not only with incident protons, but also with incident positive and negative pions, we had to weigh considerations pertaining to incident particles for all three processes before we could design the beam.

The beams were produced by accelerating protons to approximately 6.2 BeV in the Bevatron and then allowing them to impinge on a beryllium target 1/2 in. high and presenting an effective length of 2 in. to the incident proton beam. To make the optics for positive and negative particles nearly the same, this target was placed in an almost

Table I. Probability of γ-ray conversion in various regions of detector

Extent of region in polar angle θ (deg)	Solid angle subtended by region (sr)	Converter material in region	Conversion probability for one γ ray
4 to 60	3.1	0.6 cm lead 15.0 cm scintillator	87 %
60 to 147	8.4	0.6 cm lead 2.0 cm scintillator	81 %
0 to 4 147 to 180	1.1	none	0

magnetic-field-free region of the Bevatron in the west tangent tank area (Fig. 6). To facilitate positioning the target, it was placed on a probe located 20 in. from the Quadrant II magnet yoke. The target radial position was 600 3/8 inches during normal operations. To further reduce the effects of the Bevatron fringing field, the portion of the beam which passed near the magnet yoke was shielded by channeling it through an 8-in.-bore iron pipe. This pipe had a 1.0-in. wall thickness; we estimated that it reduced the magnetic field inside by a factor of about 10 from the outside field.

The secondary beam from the beryllium target was brought out of the vacuum tank through a 0.020-in.-thick stainless steel window and was collected by an 8-in.-bore quadrupole magnet (Q1 in Fig. 6). This magnet was 12 ft from the internal target and intercepted particles which were produced at a mean angle of 32 deg to the Bevatron internal proton beam. Since particles with a wide range of momenta are produced at this angle, a bending magnet (M1) was then used to provide a continuous set of dispersed images of the target at the first focus (F1). Another quadrupole magnet (Q2) provided additional focussing while a plastic scintillation counter (S1) situated at F1 electronically selected only those particles which were near the geometrical axis of the system.

Between the first focus (F1) and the second focus (F2) were two 8 in.-bore quadrupole magnets (Q3 and Q4) which provided the necessary focussing properties and a bending magnet (M2). The current in this bending magnet was set to channel particles of the desired momentum down the geometrical center of the system. The bending angle was chosen to recombine the continuous set of images at F1 into a single image at F2. A counter (S2) at F2 was used to further define the beam geometrically and to select particles of a given velocity range. Finally, a single quadrupole magnet (Q5), using the image formed at F1 as its object, focussed the beam in the region of the liquid hydrogen target. A final scintillation counter (S3) directly forward of the liquid hydrogen target further defined the beam. A list of the dimensions and optical properties of the magnets is given in Table II.

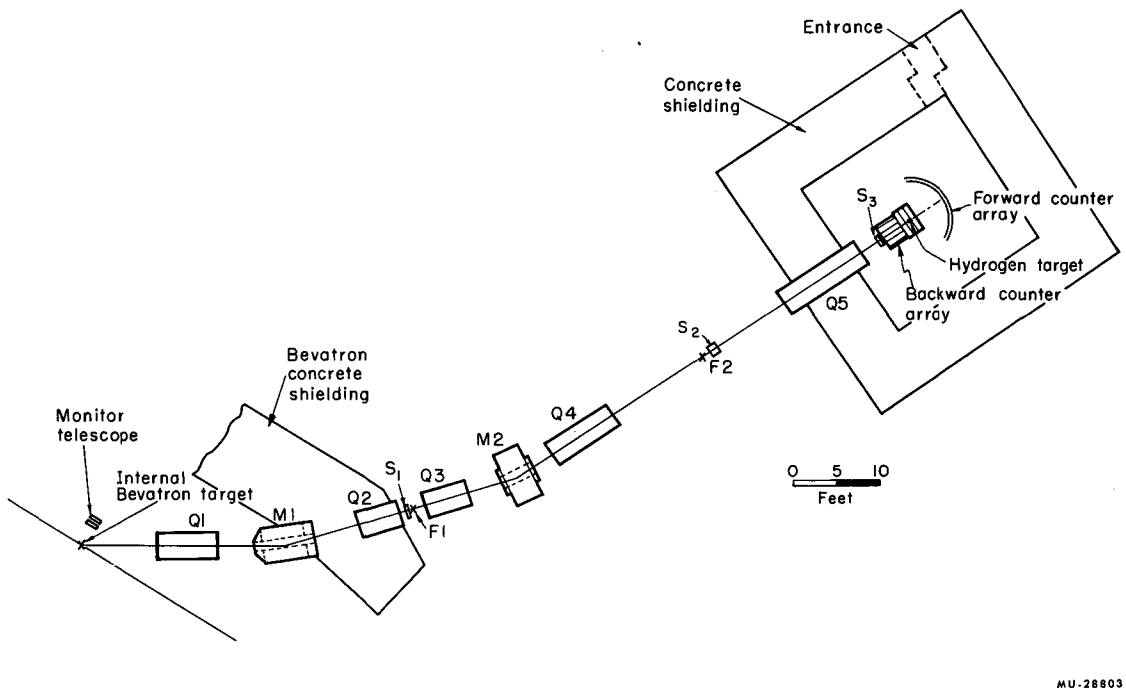

Fig. 6. Diagram of counter placement and magnet arrangement.

Table II. Description and optical properties of beam components.

Magnet	Description	Optical Properties
Q1	Two element quadrupole 8-in. bore, 32-in.-long pole faces	Front element had negative focal length in horizontal plane Rear element had positive focal length in horizontal plane
M1	Analyzer magnet 12-in. wide by 60-in. long pole faces, 4.15-in. gap	Bent beam by 17 deg
Q2	Two element quadrupole 8-in. bore, 16-in.-long pole faces	Front element had positive focal length in horizontal plane Rear element had negative focal length in horizontal plane
Q3	Same as Q2	Front element had negative focal length in horizontal plane Rear element had positive focal length in horizontal plane
M2	Analyzer magnet, "H" type 18-in. wide by 36-in.-long pole faces, 8 in. gap	Bent beam by 17 deg
Q4	Three element quadrupole 8-in. bore, end sections 16-in. long, center sections 32-in. long	Center element had negative focal length in horizontal plane End elements had positive focal length in horizontal plane
Q5	Three element quadrupole 8-in. bore, 32-in.-long pole faces	Center element had negative focal length in horizontal plane End elements had positive focal length in horizontal plane

Prior to the runs, we checked the focal and bending properties of all the magnets by using a thin current carrying wire to simulate a given momentum particle orbit.[23] Near the beginning of the experiment, the position of the internal beryllium target and the current in M1, as well as in the quadrupole magnets, were systematically varied to maximize the intensity of the transmitted beam. At these optimum settings, the intensity was measured as a function of the current in the momentum selecting magnet M2. This measurement gave 4.5% for the half width at half maximum of the momentum acceptance of the system. To minimize losses resulting from multiple scattering of the beam in the air, the entire beam path, except for small regions near the counters, was channeled through polyethylene bags filled with helium.

To indicate that a particle had possibly interacted with material in the hydrogen target, a plastic scintillation counter (S4) was placed in the 4-deg beam exit hole of the neutron detector array. This counter was in anticoincidence with the three beam counters. A comparison of this rate S1 S2 S3 $\overline{S4}$ with the coincidence rate of only the first three counters S1 S2 S3 gave an indication of the number of interactions in the target area as well as a reflection of the final image size and the prevalence of particles with improper orbits resulting from aberations in the magnets and scattering from the pole tips or gas molecules. With the flask of the target emptied of liquid hydrogen, the currents in Q5 were adjusted to minimize the ratio, S1 S2 S3 $\overline{S4}$ to S1 S2 S3. The constancy of this ratio was checked during each run and provided a good indication of magnet current drift and the behavior of the beam counters. For incident protons of 2.5 BeV/c momentum, this ratio was about 1 %.

With a circulating internal Bevatron beam of 1×10^{11} protons per pulse, about 2×10^{4} protons of 2.5 BeV/c momentum were channeled down the magnet system. The duration of this pulse was 0.2 to 0.4 seconds. As a check of the amount of internal Bevatron proton beam striking the berylium target, a coincidence between two plastic scintillation counters, set to view the target at an angle of 90 deg to the incident beam, was used as a monitor (Fig. 6).

The major contaminant of the proton beam was due to π mesons produced in the beryllium target. A clear separation between pions and protons at 2.5 BeV/c could not be made by a time-of-flight measurement alone. However such measurements were made at momenta of 0.75, 1.25, 1.50, 1.75, and 2.00 BeV/c. An extrapolation of these measurements to 2.5 BeV/c indicated that pions comprised less than 3% of the beam (Fig. 7).

Scintillation counters S1 and S3 were plastic whereas S2 was a Cyclohexene Cerenkov counter. It was used to discriminate between pions and protons for the lower momentum pion beams intended for studying the pion induced reactions at 1.75 and 1.25 BeV/c. However at a momentum of 2.5 BeV/c, this Cerenkov counter was also sensitive to protons and served no other purpose than to define the beam geometrically.

D. Electronics

The electronic circuitry can be divided into three sections: the primary trigger circuit, the neutron timing circuit, and the storage and magnetic-tape read-out circuit. Only a brief general description of these will be given here since detailed accounts have already been published elsewhere.[8-13] A detailed description of the many adjustment procedures and tests of the timing of the electronics and the integration of all the component sections during the actual run is given by Auerbach.[5]

The trigger circuit indicated that an interaction, which had produced a slow secondary particle, had taken place in the hydrogen target by requiring a properly timed coincidence with the beam counters S1 S2 S3, and an anticoincidence with S4. A signal was generated by this combination which opened a gate whose boundaries were sufficiently broad to include all neutrons whose flight times would correspond to the neutron energies of interest. If, while this gate was open, a signal was found on any of the neutron counters, a trigger signal was formed which actuated our neutron timing circuit (the Chronotron).

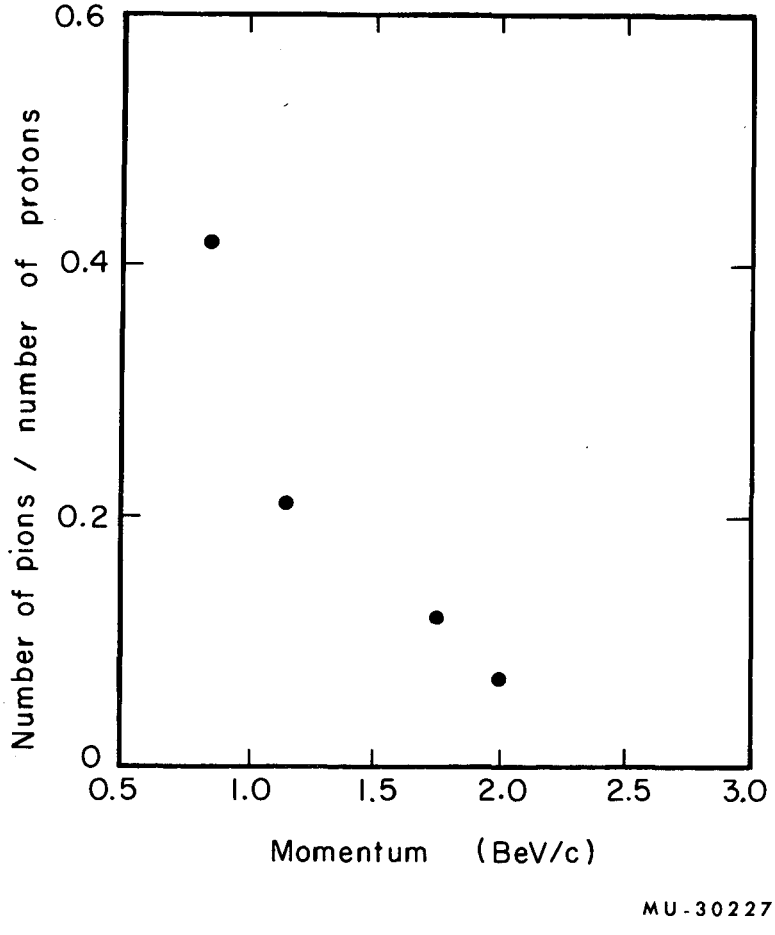

Fig. 7. Measured ratios of positive pions to protons in incident beam as a function of beam momentum. This beam was extracted at an angle of 32 deg. from the Bevatron circulating beam.

The Chronotron was a circuit which compared the time difference between two input pulses, and, depending on the magnitude of this difference, responded with an output pulse in one of seven channels.[11] In this case, the two pulses compared were a pulse derived from the beam counter coincidence, t_0, and a later pulse from one of the neutron counters. Figure 8 is a simplified diagram of the overall trigger system. Four separate Chronotrons were actually incorporated into the electronics, one for the neutron detectors of each quadrant shown in Fig. 4; they are referred to in the diagrams as α, β, γ, and δ.

Although the trigger system could have been made more selective, we decided rather than try to add other criteria to it (thus perhaps further compounding the systematic corrections) to record all the events which gave triggers and sort them later on a high speed digital computer. All events which satisfied the trigger requirements were recorded; this included the counter numbers of all fast and slow particles as well as the timing measurements of the slow particles. These numbers were recorded in a magnetic-core storage unit of 1600 bit capacity.[13] After ten of these events were stored, the entire contents of the core memory was transferred to magnetic tape. In normal operation, the Bevatron beam pulse was long enough to allow core to be read out 4 to 6 times per pulse. The magnetic tape format was directly acceptable by an IBM 709 or 7090 computer; hence, each event could be electronically examined to ascertain that it contained the proper number of fast and slow particles, and, after satisfying this criterion, the event could then be checked for energy and momentum balance.

The efficiency for counting neutrons of a given energy for each of the Chronotron's channels is shown in Fig. 9. Table III is a list of the mean neutron energies and widths of the seven time bins as derived from the curves of Fig. 9. Much effort was expended in determining these efficiency curves and in assuring ourselves that all of the neutron counters had the same efficiency throughout the run. Appendix B is a more detailed discussion of this matter.

The setting and adjustment of the neutron time-bin positions and widths was done using fast ($\beta \simeq 1$) charged particles and then making

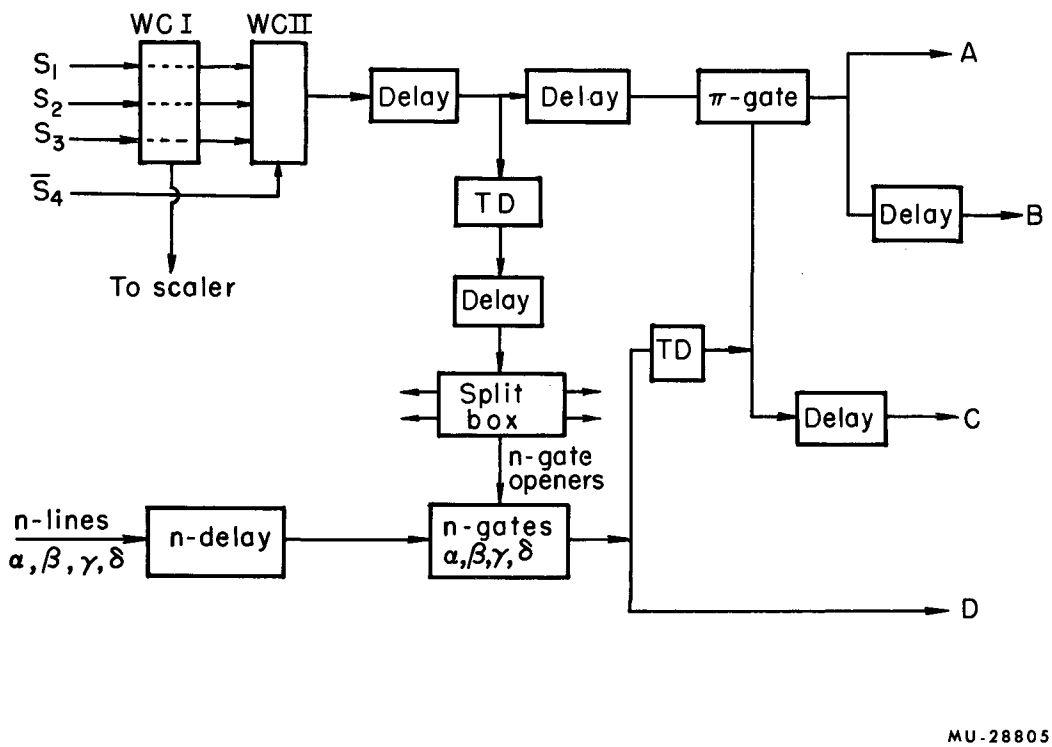

Fig. 8. Simplified diagram of overall trigger system. From point A, the signal goes to the Chronotron, where it provides the zero reference time τ_0 corresponding to the flight time of a pion, with $\beta = 1$, between target and dish. From B, the signal goes to gate-generator units which provide pulses that gate on the pion CD units. From C, the neutron CD units are gated on. From D, the signal goes to the Chronotron to give the neutron timing τ_n compared with the reference signal τ_0.

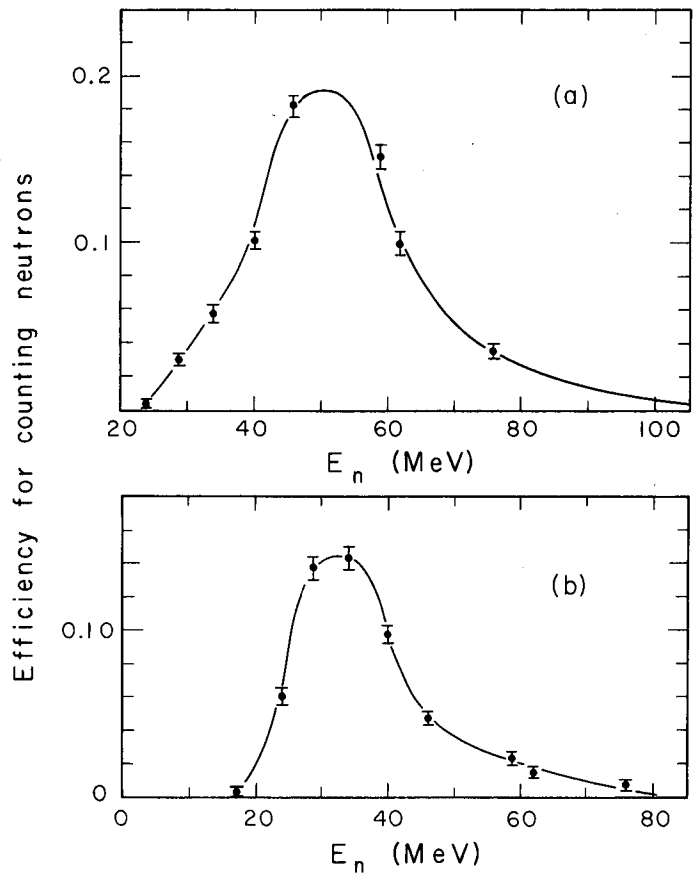

MU-28807

Fig. 9. Neutron counting efficiency η as a function of incident neutron kinetic energy E_n.

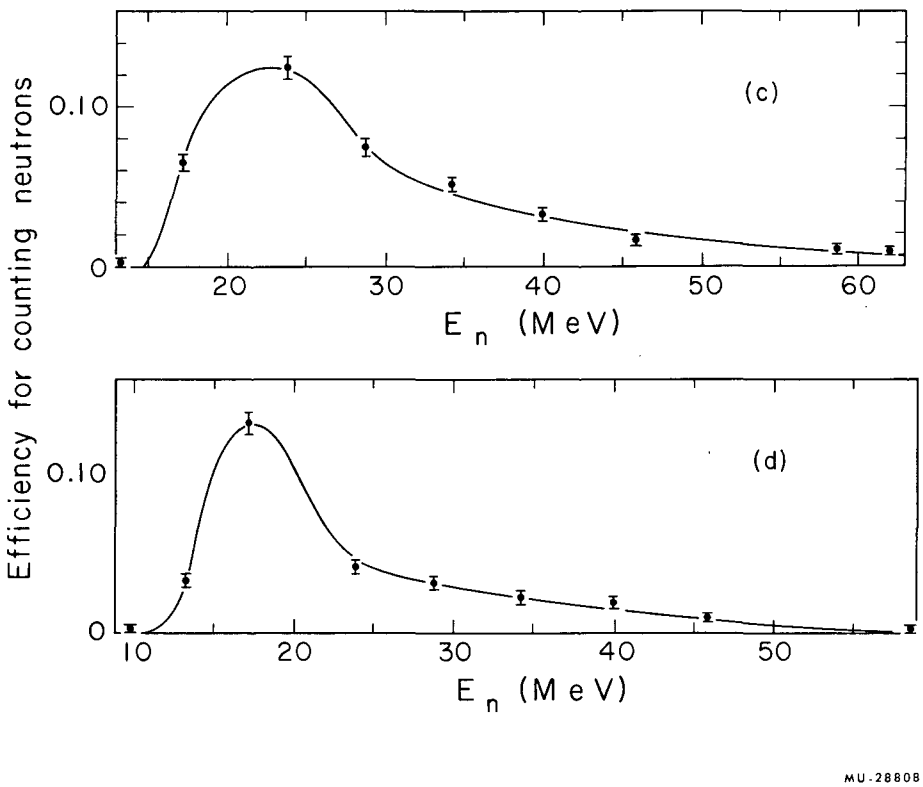
Efficiency for counting neutrons
0.10
0
(c)
20
30
40
50
60
E n (MeV)
0.10
0
(d)
10
20
30
40
50
E n (MeV)
MU-28808

Fig. 9. (Cont.)

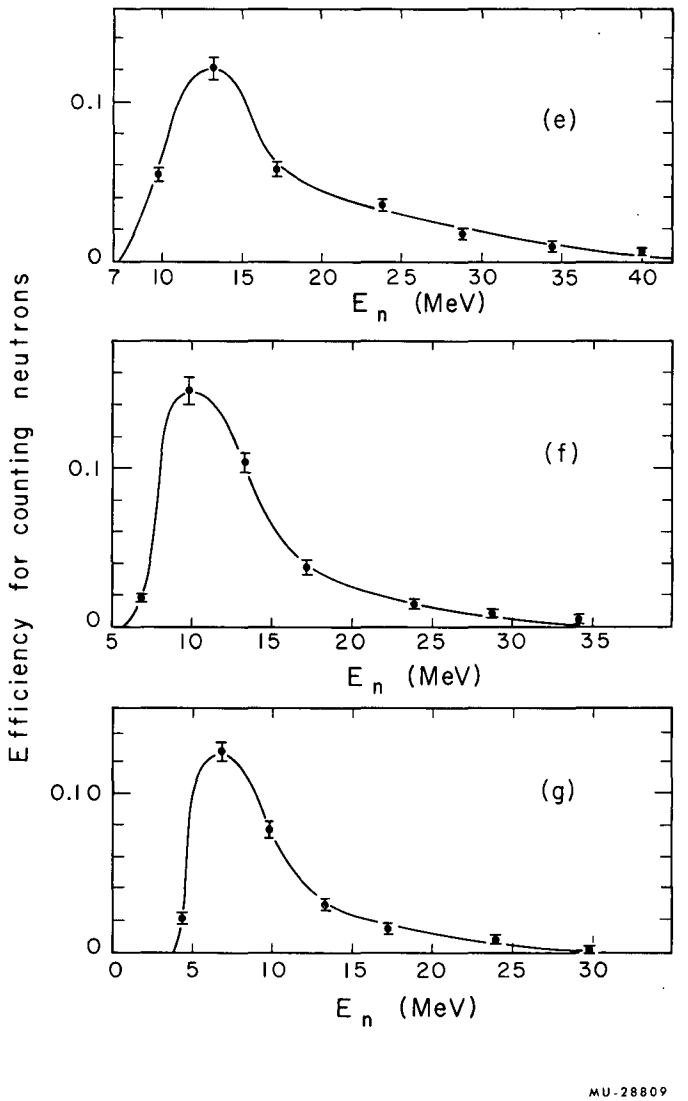
Efficiency for counting neutrons
0.1
0
7 10 15 20 25 30 35 40
E n (MeV)
(e)
0.1
0
5 10 15 20 25 30 35
E n (MeV)
(f)
0.10
0
0 5 10 15 20 25 30
E n (MeV)
(g)
MU-28809

Fig. 9. (Cont.)

Table III. Values of mean energy and mean $(p/\mu)^2$ for seven time-of-flight intervals.

Time bin	Mean energy T_{2L} and rms width (MeV)	Mean $(p/\mu)^2$ and rms width
τ_1	54 ± 14	5.2 ± 1.3
τ_2	38 ± 12	3.6 ± 1.1
τ_3	29 ± 10	2.8 ± 1.0
τ_4	23 ± 8	2.2 ± 0.8
τ_5	18 ± 7	1.7 ± 0.7
τ_6	13 ± 5	1.3 ± 0.5
τ_7	10 ± 5	1.0 ± 0.5

the change in cable lengths to correspond to the slower neutrons. This was accomplished by inserting a delay equal to the difference in flight time between a particle with $\beta \simeq 1$ and a time bin 1 neutron in the neutron lines. The flight difference was the 160 cm distance between the hydrogen target and neutron detectors. Using this procedure the various gates as well as the positions and widths of the time bins could be set. Figure 7 of reference 5 depicts some timing curves done using this procedure.

The relative timing of the individual counters was done by means of a pulsed nsec light source[12] which could be inserted into the front of each scintillator. Using this source the relative delay of each counter could be determined to ± 0.2 nsec.

Since the absolute widths of the Chronotron channels could only be set to within ± 0.2 nsec, this contributed to a statistical uncertainty of the integrated efficiencies (discussed in Sec. V–C). This effect was most serious for time bin 1 where it amounted to 7.1% of its nominal width but was inconsequential compared to the counting statistics in the slower bins, being only a 2.9% effect in time bin 7. In any comparison of data from different time bins this effect has been included by combining it with the counting statistics as a source of uncertainty.

IV. RAW DATA

In this section a presentation of the raw data without corrections for geometrical or instrumental biases is made. Since some of these corrections are large and quite complicated, a presentation of the pristine data is useful if for no other purpose than as an introductory orientation.

Measurements were made with two target conditions — flask full and flask empty — and two delay conditions — normal and abnormal. To achieve the abnormal delay conditions, sufficient delay was added to the neutron channels so that any slow particles detected would have had to traverse the flight path with $\beta > 1$ to be correlated with the fast particles. This condition gave a measurement of the purely accidental neutron background. The target flask was also emptied of hydrogen and runs were made to estimate the contribution to the apparent cross section from background reactions occurring in the target walls. In terms of the four possible target and delay conditions — full-normal, empty-normal, full-abnormal, and empty-abnormal — the net cross sections are given by

$$\sigma_N = \sigma_{FN} - \sigma_{EN} - \sigma_{FA} + \sigma_{EA} ,$$

where the individual cross sections are defined in the usual way as

$$\sigma = \frac{N_c}{\rho L A_0 N_i} .$$

The constants involved are:

N_c = number of events,
ρ = density of liquid hydrogen[6] = 0.0708 g/cm^3,
L = length of the hydrogen target in the beam direction = 10 cm ,
A_0 = Avogadro's constant[16] = 6.0249×10^{23} (g-mole)$^{-1}$,
and
N_i = number of incident beam particles.

Table IV gives the number of protons incident on the target for these four target and delay conditions. Also given as an indication of the magnitude of the selection done by the electronics and the computer fitting program are the trigger rate (defined in Sec. III-D), the number of these triggers which consisted of only two fast particles and one slow particle, and finally the number of these triggers which satisfied the kinematics of our reaction. In this table a summation has been made of events from all of the seven neutron time bins and the seven theta zones.

Table V is a breakdown of the events which were accepted by the computer fitting program according to the time bin and theta zone of the neutron. Background subtractions were made on the individual bins in a manner similar to that applied to the total data. The first number listed for each bin is the number of events with the target-delay conditions full-normal; the second, empty-normal; the third, full-abnormal; the fourth, empty-abnormal. Following these is the raw cross section in μb for the bin, the errors presented being due to counting statistics only. No efficiencies or geometrical corrections are included in this data.

Table IV. Raw data summary: Events summed over all neutron time bins and theta zones.

		Full-normal	Empty-normal	Full-abnormal	Empty-abnormal	Net cross section
Number of incident protons	$\times 10^6$	69.45	29.87	23.76	11.29	
Triggers (see Sec. III-D)	$\times 10^3$	535.6	122.1	7.0	1.6	
	σ (mb)	7.71	4.09	0.35	0.15	3.42
Events with only two fast particles and one slow particle	$\times 10^3$	72.0	11.6	1.6	0.2	
	σ (mb)	1.04	0.39	0.07	0.02	0.60
Events with only two fast particles and one slow particle which fit the kinematics of reaction: $p + p \rightarrow n + p + \pi^+$		16,337	1,132	166	13	
	σ (mb)	0.235	0.038	0.007	0.001	0.191

Table V. Raw data: Neutron distribution in time bin and theta zone.

	θ_1	θ_2	θ_3	θ_4	θ_5	θ_6	θ_7
	304	422	525	533	807	1120	652
	41	50	61	52	53	56	53
t_1	5	1	9	8	3	3	3
	0	0	0	0	0	0	0
	2.7 ± 0.3	4.3 ± 0.4	5.1 ± 0.4	5.5 ± 0.4	9.6 ± 0.5	13.9 ± 0.5	7.4 ± 0.4
	283	346	460	611	900	1032	446
	37	22	40	52	37	46	26
t_2	7	2	6	5	5	5	1
	0	0	0	3	0	0	0
	2.5 ± 0.3	4.1 ± 0.3	5.0 ± 0.4	7.0 ± 0.5	11.3 ± 0.5	12.9 ± 0.5	5.4 ± 0.4
	183	224	380	499	613	565	261
	19	16	23	23	27	38	15
t_3	1	3	2	2	3	1	3
	0	0	1	0	0	0	0
	1.9 ± 0.2	2.5 ± 0.3	4.6 ± 0.3	6.2 ± 0.4	7.7 ± 0.4	6.7 ± 0.4	3.1 ± 0.3
	157	232	377	476	450	358	167
	11	17	13	20	18	23	23
t_4	4	1	5	5	1	5	3
	0	0	0	0	1	1	1
	1.7 ± 0.2	2.7 ± 0.3	4.7 ± 0.3	5.9 ± 0.4	5.8 ± 0.3	4.2 ± 0.3	1.6 ± 0.3
	108	149	261	293	245	177	94
	9	12	13	13	19	13	10
t_5	4	3	3	4	2	0	0
	1	0	0	1	0	0	0
	1.1 ± 0.2	1.6 ± 0.2	3.1 ± 0.2	3.6 ± 0.2	2.8 ± 0.3	2.1 ± 0.2	1.0 ± 0.2
	109	186	254	223	197	114	60
	12	8	16	14	19	8	9
t_6	4	3	5	7	2	3	1
	1	0	0	1	0	1	1
	1.1 ± 0.2	2.3 ± 0.2	2.9 ± 0.3	2.5 ± 0.3	2.1 ± 0.3	1.3 ± 0.2	0.6 ± 0.2
	62	79	101	96	84	41	21
	7	4	12	9	4	6	3
t_7	3	2	3	8	1	2	4
	0	0	0	0	0	0	0
	0.5 ± 0.2	0.9 ± 0.2	0.9 ± 0.2	0.7 ± 0.2	1.0 ± 0.2	0.3 ± 0.2	0.0 ± 0.0

V. SYSTEMATIC CORRECTIONS

A. Sources and Description

A number of corrections must be made to the data presented in the previous section before any comparisons of data with the theoretical models can be made. What follows is a description of the major instrumental biases whose explicit evaluation will be undertaken in succeeding sections.

1. Neutron Detection Efficiency

Neutron detection efficiency has been determined in a subsidiary experiment published elsewhere.[14] However, a brief description of the method used is given in Appendix B, and the neutron counting efficiency as a function of neutron energy for each of the seven time bins is shown in Fig. 9. It is these curves which have been incorporated into the subsequent analysis and which have been used to compute the mean neutron energy and the rms width of each of the bins shown in Table III.

2. Kinematical Fitting Program

The fitting program selected from the events which had two fast particles ($\beta \simeq 1$) and one slow particle (defined as a count in one of the seven Chronotron time bins) those events which fitted the kinematics of the reaction

$$p + p \rightarrow n + p + \pi^+$$

at an incident proton momentum of 2.5 BeV/c within the resolution limits of the detection apparatus. Because of the geometrical shape of the scintillation counters and the size of the neutron time bins, events occurring in them will not have their measured parameters normally distributed about a mean, hence the applicability of the usual goodness-of-fit criteria such as the χ^2 test should not be expected. With this in mind a search program was designed which would attempt to make a rigorous fit of each event to the kinematics of the single-pion production

reaction within the resolution limits set by the detection apparatus. If such a fit was made, the event was accepted as representative of this reaction; if not, the event was rejected as background. A more detailed account of these considerations and of the operation of the search program than will be given here is presented by Johnson.[4]

Seven final-state quantities were measured; the polar and azimuthal angles of all three final-state particles, and, by means of its flight time, the neutron's momentum. Since the initial beam momentum is known, the only remaining unknown quantities in the set of four equations representing energy and momentum balance (Eqs. II-1) are the two momenta, $q_{1'L}$ and $q_{\mu L}$, of the nonspectator particles. These variables can be eliminated from these four equations leaving two equations which can then be solved for the pion angular coordinates $\theta_{\mu L}$ and $\phi_{\mu L}$. These can be expressed as functions whose arguments are measured quantities only:

$$\theta_{\mu L} = F_1 (q_{1L}, q_{3L}, \theta_{3L}, \phi_{3L}, \theta_{1'L}, \phi_{1'L}) ,$$

and

$$\phi_{\mu L} = F_2 (q_{1L}, q_{3L}, \theta_{3L}, \phi_{3L}, \theta_{1'L}, \phi_{1'L}) .$$

In an attempt to bring F_1 and F_2 simultaneously within the resolution limits of $\theta_{\mu L}$ and $\phi_{\mu L}$, the fitting code varies the values of the arguments of F_1 and F_2 within the ranges imposed by the scintillator geometry and the time bin sizes. If this can be done the event is accepted as a valid example of the single pion production reaction under study. If after a predetermined number of searches a fit cannot be made, the event is rejected as arising from a background reaction.

The search procedure for the fitting code is begun by computing F_1 and F_2 using the central values for their arguments. If this did not give values of $\theta_{\mu L}$ and $\phi_{\mu L}$ within the geometrical limits of the counter, then the gradients of F_1 and F_2 with respect to their arguments were computed and a change was made in the arguments of F_1 and F_2, consistent with the resolution of the apparatus, in a direction, given by the

gradients, which would lead to values of F_1 and F_2 within the resolution of the system. As soon as values of F_1 and F_2 were found which satisfied the resolution requirements, the searched values for the angles and momenta of all particles involved were recorded and the event accepted. From these values, which give a complete set of consistent kinematics for all particles involved in the reaction, one computes a set of center-of-mass scattering angles for the nonspectator particles making use of the transformations given in Appendix A.

A complication arises because one has no a priori knowledge which of the two fast particles is the proton and which is the pion. Thus, the search program must attempt to make a kinematical fit with first one assumption and then the other. In about 18% of the total accepted events, a fit can be made with either assumption. For the nonspectator particles associated with these ambiguous events there will be no unique set of barycentric scattering angles θ^* and ϕ^*. Fortunately this complication arises for only a relatively small number of events and, for this sample, the complication is limited to a discrete and well defined range of the variables θ^* and ϕ^*, and most can be excluded from the analysis. Physically, these events correspond to cases where the pion and the proton are moving forward in the laboratory and have nearly the same polar angle.

The two most important questions concerning the search code which must be answered before a meaningful analysis can be made are, (a) what is the code's efficiency in accepting events resulting from our reaction of interest, and (b) what is its effectiveness in rejecting events arising from background reactions.

3. Geometrical Corrections

The most serious geometrical corrections arise from the nucleon's strong preferential emission in the forward laboratory direction. Hence, the number of nucleons which escape through the polar 4-deg hole in the detectors cannot be neglected. Spectator neutrons lost through this aperture represent only a loss in counting rate and a small limitation on the range of the variable W^2 since the cross sections which are being measured are normalized to the number of neutrons per

P^2 and per W^2 interval. The loss of the nonspectator proton associated with each event is a serious consideration since this loss will occur in approximately 25% of all events and is a function of both P^2 and W^2 as well as being a function of the angular distributions in θ^* and ϕ^*. Since the kinematics of this three-body final-state reaction do not force the pion to be emitted as preferentially forward as the proton, its corresponding correction is not nearly as large. However, the pions can be emitted in the backward direction thereby introducing an additional bias since the scintillation detectors extend only to 147 deg in polar angle. Since the most serious of these corrections involve the nonspectator proton emitted in the forward direction, any attempt at a correction should include the effects of the size of the liquid hydrogen target and size of the incident proton beam.

4. Overlap and Range Corrections

Both overlap and range corrections are relatively minor. The first arises because of the finite size of the counters and the possibility of any two of the three final-state particles falling into the same counter. Although in principle it might have been possible to distinguish the pions and protons from the slow neutrons if they arrived in the same counter, the identification of the small neutron pulse so soon after the large charged-particle pulse could not be done without special effort and was not attempted. If both fast particles fell into the same counter the event would be rejected because it would appear to have only one nonspectator particle.

Because of the 0.6 cm of lead covering the scintillators, a minimum range requirement was imposed on the charged particles that were counted. This meant that the detected protons must have had at least 400 MeV/c and the pions at least 110 MeV/c of momentum.

5. Scattering Corrections

Corrections to the data to account for the scattering of any of the three final-state particles must also be made.

The most serious of these scattering corrections arises because of events lost as a result of one of the two fast particles interacting with

the thick neutron counters to produce secondary particles that trigger adjacent counters. These events would be rejected because of an apparent excess of fast particles.

The second of these scattering corrections arises because of the large and strongly energy dependent cross section for the scattering of low energy neutrons on hydrogen. Thus, neutrons produced in the liquid hydrogen target may also be scattered in the target and might then possibly be detected by the neutron counters. The number of such events accepted will be a strong function of the neutron energy and the sensitivity of the search program to such changes of neutron energy and angle.

Two other scattering processes occur. A neutron may scatter in a neutron counter, triggering it, and then still have sufficient energy to also trigger an adjacent counter. Finally a fast particle may interact with the liquid hydrogen of the target and be lost. Both of these processes are much smaller than the first two and will be neglected.

B. The Monte Carlo Comparison — DRYLAB

To investigate and evaluate the effects of the complex counter geometry, the neutron timing resolution, the incident beam and target size, as well as the biases of the search code, we attempted to simulate the entire apparatus by using Monte Carlo techniques coupled with a high speed digital computer. With this one code — suitably christened DRYLAB — it was hoped that for each of the 49 data bins defined by the 7 neutron theta zones and the 7 neutron time channels a reliable estimate could be made of the size of these bins in the variables P^2 and W^2 as well as an estimate of their efficiency for counting events within these limits. Furthermore, a detailed investigation could be made of the effects of the 4 deg beam exit hole and the ambiguity introduced by the indistinguishability of the nonspectator particles in some of the events.

The code generated events having kinematics representative of our reaction of interest weighted by the measured or estimated initial distributions. The trajectories of the particles were followed through the detection apparatus where on the basis of random number generators

and the measured detection efficiency a decision was made as to whether the event would be counted. If it was decided that the event would have been detected, its counter and time bin configuration were noted and the event transferred to a subroutine containing the search code. An attempt was then made to fit this counter configuration to the production reaction under study just as was done with the events generated by the Bevatron. From this, a direct estimate could be made of the search-program efficiency. For all the events at this stage the initial kinematical values as well as the values found by the search code were recorded on magnetic tape to be later sorted and evaluated.

Since, to a very great extent, the analysis of this experiment depends on this code, it is worthwhile to describe in detail its operation and in what ways it contributed to the understanding of how the complicated instrumental resolutions shaped the data. Let us then, step by step noting explicitly the assumptions made, trace the operation of this code.

(1) Since the primary analysis was to be done in terms of the variables P^2 and W^2, DRYLAB began by selecting values of these variables with an equal probability between their extreme limits as seen by the apparatus:

$$0.38 < p^2/\mu^2 < 10.59$$

and

$$59.54 < W^2/\mu^2 < 121.25 .$$

(2) From the value of P^2, the kinetic energy of the neutron, T_{3L}, was computed, and the efficiency for counting in each of the seven time bins at this value of T_{3L} was determined from the measured efficiency curves shown in Fig. 9. On the basis of a random number generated with equal probability between 0 and 1 and the total neutron-detection efficiency, a choice was made as to whether the neutron was detected; the choice as to which of the seven time bins it entered was decided on the basis of their relative efficiencies. If the neutron was not counted the code returned to Step 1.

(3) A value of the incident beam momentum was now chosen. The choice was based on a Gaussian distribution having a half width at half maximum of ± 4.5% centered about an incident momentum of 2.5 BeV/c. The kinematics of the reaction depended only weakly on this distribution and a considerably larger momentum bite could have been tolerated.

(4) Having fixed the incident momentum, q_{1L}, as well as P^2 and W^2, we now determined the neutron angle, θ_{3L}, from the relation

$$\cos(\theta_{3L}) = \frac{W^2 - (W_{1L} + M_2 - M_3 - T_{3L})^2 + q_{1L}^2 + q_{3L}^2}{2\, q_{1L}\, q_{3L}}$$

(see Appendix A). For an arbitrary choice of the variables q_{1L}, P^2, and W^2, there need not be any corresponding physical value for $\cos(\theta_{3L})$. Indeed for these values the magnitude of $\cos(\theta_{3L})$ is greater than 1, signifying that a choice inconsistent with energy and momentum balance has been made. If this is the case the code abandons the event and returns to Step 1.

(5) A point in the liquid hydrogen target was now chosen in which the interaction was assumed to have taken place. The spatial distribution of the incident beam was assumed Gaussian with a half width at half maximum of 1 in. The choice of interaction point was made consistent with the target geometry described in Sec. III-A.

(6) The neutron azimuthal angle, ϕ_{3L}, was now selected on the assumption of a uniform distribution between 0 and 360 deg.

(7) The neutron trajectory from the interaction point in the hydrogen target was now calculated and the counter in the detection array which it triggered determined. If the neutron was found to miss the detectors — that is, if it didn't have a polar angle in the region 4 to 60 deg measured from the center of the hydrogen target — the event was abandoned and the code returned to Step 1.

(8) The remaining kinematical angular variables for the non-spectator particles was now chosen. Since, for these particles, the distributions of interest involve their angles measured in their center

of mass frame, θ^* and ϕ^*, the selection was made in this frame on the basis of a uniform distribution in ϕ^* and $\cos(\theta^*)$. In this frame the directions of the two particles are colinear and opposite, the determination of these angles for one of the particles fixes those of the other.

(9) The nonspectators momentum vectors were now transformed from their own center of mass frame to the laboratory frame again using the transformations described in Appendix A. The trajectories of the particles were followed to determine which of the counters in the detection array were triggered. If either particle missed the array — had a polar angle outside of the region from 4 to 147 deg measured from the center of hydrogen target — the event was abandoned and the code reverted to Step 1.

(10) A requirement was now placed on the laboratory momentum of the nonspectator particles. The event was abandoned if the pion had less than 110 MeV/c or the proton less than 400 MeV/c of momentum. This ensured that both particles could penetrate the 0.6 cm of lead covering the scintillation counters.

(11) A final requirement was that no two of the three final-state particles land in the same counter. If they did, the event was discarded and the code returned to Step 1.

If the event fulfilled this and all of the previous requirements, we assumed it to be a valid statistical representation of the kinematics of the production process under investigation and, hopefully that it was representative of the events recorded by the detection apparatus.

(12) The time bin of the neutron and the counter configuration of all the particles was now transferred to the search code. This was exactly the same starting point the search code would have had for a real event generated at the Bevatron and exactly the same attempt would be made to fit this Monte Carlo generated event to our three-body final-state reaction. A fitting attempt was made with both assumptions as to which of the nonspectator particles was the pion and which the proton.

(13) If the search code succeeded in fitting the event to either or both of the above hypotheses, then from the fitted values of the

momentum vectors of the particles, the angles of the nonspectators in their own center of mass frame, θ^* and ϕ^*, were computed.

(14) On magnetic tape we recorded the initial coordinates of each event consisting of P^2, W^2, ϕ_{3L}, $\cos(\theta^*)$, ϕ^*, q_{1L}, the target interaction point, as well as the time bin and Chronotron channel which the event triggered, along with the search program results consisting of whether the search was successful or not, the fitted values of P^2, W^2, $\cos(\theta^*)$, ϕ^*, and q_{1L}.

Each section of DRYLAB was coded as one or more subroutines, all being connected by a main calling program. This greatly facillitated debugging and allowed each subroutine to be tested independently of the others and independently of the main code to ensure that the subroutines were indeed generating events weighted by the desired distributions. For economy of machine operation, most of the subroutines were coded in FAP,[21] but the main calling program and some of the subroutines were coded in FORTRAN.[22] An IBM 7090 was used for the computation. The magnetic tape output was written in binary records, each record consisting of 30 events. The output was completely buffered so that tape writing was done simultaneously with computation. About 160,000 events per hour were selected at Step 1 corresponding to 10,000 events per hour which would have given legitimate counts in the detection apparatus.

As is all such Monte Carlo calculations, the entire structure rests on the random number generator. All random number generators used in conjunction with modern high speed computers operate by means of a recursion relation of the form

$$R_{n+1} = F(R_n)$$

where R_{n+1} is the $(n+1)$th random number generated and F is some function of the previous random number, R_n. Of course such a formula, by its very nature, cannot give true random numbers — — this is, successive values of R_n which are uncorrelated. However, by an appropriate choice of the function, F, these correlations may be reduced

to a point where the numbers produced closely approximate a random distribution. A generator of the power residue type[24] which employed the recursion relationship

$$R_{n+1} = C\, R_n \text{ (module } 2^{35}\text{)}$$

where C is an appropriately chosen constant, was ultimately incorporated into DRYLAB. In the actual computation, five independent generators of this type were used, all with different values of the constant, C, and the initial values of R_1. To minimize correlations yet further, none of these five generators was ever called consecutively. As a final check, DRYLAB was partially rerun with a standard library routine random number generator.[25] Within the Monte Carlo statistics, the two results were in excellent agreement.

The first facet of the experiment to be investigated with the aid of DRYLAB was that of overall detection efficiency and the rejection of background events. In order to rigorously include all possible events which could have occurred from our reaction, the search code should be allowed to roam the entire limits of the time bins -- even though the detection efficiency near the ends of the long high energy tails is quite small. Also one would have to let the search continue through not only the polar and azimuthal angular limits of the scintillation detectors as seen from the center of the hydrogen target, but through the limits as seen from any extreme point in the finite sized target. One would also be required to allow the code to take as many steps as necessary, each time computing a new set of gradients, in order to either find a solution or reach a stalemate. Two reasons indicate caution in adopting the above philosophy. The first is whether the increase in calculational time which would come about primarily through extending the number of allowable searches is justified given the expense of computer operation. The second much more serious reason is whether such a search procedure (given the limited resolution of the detection apparatus) would allow an appreciable number of events to be accepted which arise from background reactions. Since we have a great many triggers which have the requisite number of fast and slow particles, it was

feared that such a liberal search procedure would allow a considerable fraction of these events to be accepted even though they did not originate from the reaction under study.

The first of these two questions can be answered rather easily. It was found that the cross sections measured at the Bevatron did not change appreciably if the number of searches was increased above 10. Explicitly, if the number of searches was increased from 10 to 20, the overall cross section changed by less than 1%. Thus 10 was adopted as the number of searches to be made; when these were exhausted the event was rejected as due to background.

Since DRYLAB allows us to estimate the efficiency with which events having the kinematics of our reaction are accepted, we also have a method for dealing with the second question concerning background. If the size of the regions in which the search code is allowed to hunt are varied, then DRYLAB will indicate how the corresponding efficiency will change. If we then allow the search code to attempt to fit real events generated by the Bevatron with the same sized search regions, the Bevatron cross sections should be directly proportional to the DRYLAB efficiencies if the Bevatron events have the same kinematical form as those generated in DRYLAB. Of course, we assume that the distributions built into DRYLAB are reasonable -- though not necessarily exact -- approximations to those of the actual production reaction.

One of the 12 magnetic tapes containing about 8.5% of the total data recorded at the Bevatron was analyzed with various limits imposed on the search code. DRYLAB was run at the corresponding condition for sufficient time to determine a statistically reliable efficiency. The efficiency as determined from DRYLAB was taken as the ratio of the number of events which were accepted by the search code to those which would have been recorded by the detection apparatus. In the step by step description of DRYLAB this corresponds to the ratio of the number of events fitted by the code at Step 13 to those which would have triggered the apparatus at Step 11. Figure 10 shows the results. Reading from right to left the points correspond to the search code conditions described below.

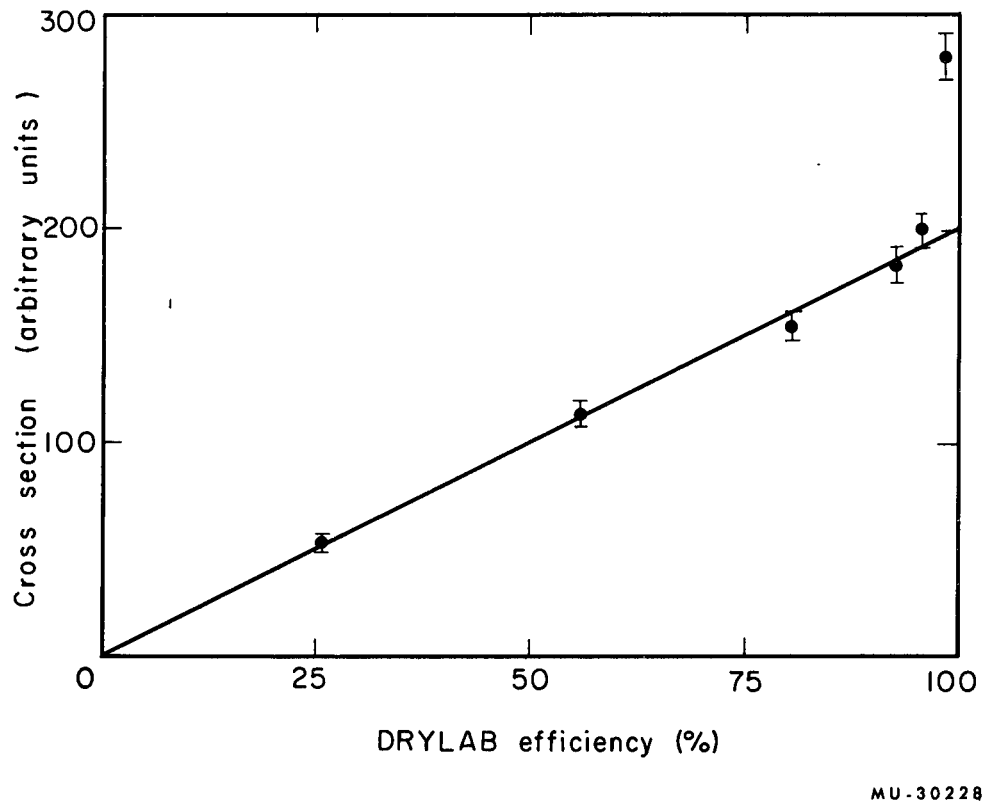

Fig. 10. DRYLAB efficiency as a function of search code limits.

Point 1. Here the search code was allowed to go to the extreme limits of the time bins as shown in Fig. 8. The scintillation counter sizes were defined by the extreme angles, both polar and azimuthal, intercepted by the counter from any point in the target.

Point 2. The time bin sizes were reduced to between the points where the detection efficiency fell to 1/2 its maximum value as given in Fig. 8. A point target was assumed for the determination of the maximum polar angle subtended by the scintillators. The azimuthal angular limits were as in Point 1.

Point 3. A point target was assumed for both the polar and azimuthal limits of the counter dimensions. The time bin sizes were as in Point 2.

Point 4. The central angles intercepted by the counter were unchanged from Point 3, but the angle subtended in both the polar and azimuthal directions was reduced by 25%. The time bin sizes were the same as in Point 2.

Point 5. The same as Point 4 except that the subtended angles were reduced by 50%.

Point 6. The same as Point 4 except that the subtended angles were reduced by 75 %.

Except for the top point the plot shows remarkable linearity, and on this basis a decision was made to continue the analysis using the angular sizes of the counters defined by a point target and time bin widths corresponding to where the efficiencies fell to 1/2 their maximum value. These were the conditions of Point 3 and all of the subsequent analysis was done with these search program limits as was the data presented in Tables IV and V.

To accumulate better statistics DRYLAB was now run with the above search program limits until about 10^5 events were generated which would have triggered the apparatus. This ensured that the statistical errors in the Monte Carlo calculation were small compared to those in the Bevatron data. All of these events were combined to form one high density magnetic tape (800 bits/in.) This tape, containing almost 3 million numbers of 36 bits each, could be read and sorted in 5 to 10 minutes on the Lawrence Radiation Laboratory's IBM 7090

computer. Table VI is a tabulation of some of DRYLAB's results from which we can make a number of pertinent conclusions.

(1) The search code has a reasonably high efficiency, 92%, for fitting events originating from our reaction. Futhermore, when it asserts that it has distinguished the nonspectator pion from the nonspectator proton, it has made the correct assignment for 99% of the events. We also see that for 17.6% of the total events it has successfully fitted, the resolution of the apparatus was not sufficient for it to identify the nonspectator particles. This agrees extremely well with the corresponding ratio of 17.4% derived from real events detected at the Bevatron. Again our faith that DRYLAB is a reasonable representation of the experiment is bolstered.

(2) The number of events lost because particles did not have sufficient momentum to penetrate the 0.6 cm of lead covering the counters is a small correction to the total data.

(3) The number of events lost because two or more particles entered the same counter is also only a small correction.

Next, with the aid of the 10^5 DRYLAB events, a study was made of how the search code and the form of the detection apparatus shaped the kinematical regions of the reaction which were accessible to us. For this study the on-line cathode-ray-tube plotter (CRT) of the Lawrence Radiation Laboratory's IBM 7090 computer proved extremely useful. Figure 11 is a plot of the P^2, W^2 distribution of the 10^5 DRYLAB events which were fitted by the search code. Figure 11a is the distribution in terms of the initial values of these variables; Fig. 11b is the distribution in the same variables computed from the search program fit to these events. Since the initial distribution in these variables assumed in Step 1 of DRYLAB was one of uniformity within the region bordered by the square, Fig. 11a shows how the apparatus selected the events which triggered the detector and Fig. 11b indicates how the search code distorted the distribution given by Fig. 11a in attempting to make a fit. The search code tends to cluster the original smooth distribution because of the limited resolution of the detection apparatus; this tendency indicates that any detailed sorting of

Table VI. DRYLAB event summary.

		Number	Fraction
1.	Events tried at Step 1 of DRYLAB	1,704,952	
2.	Events counted by detection apparatus	103,920	6.10% of events tried
3a.	Events accepted by search code	95,359	91.76% of events counted
3b.	Pion and proton correctly distinguished	77,732	81.51% of events accepted
3c.	Pion and proton incorrectly distinguished	847	0.89% of events accepted
3d.	Pion and proton not distinguished	16,780	17.60% of events accepted
4a.	Events lost because of insufficient pion momentum	2,553	2.46% of events accepted
4b.	Events lost because of insufficient proton momentum	0	
5a.	Events lost because proton and neutron in same counter	351	0.34% of events accepted
5b.	Events lost because pion and neutron in same counter	789	0.76% of events accepted
5c.	Events lost because pion and proton in same counter	1,755	1.69% of events accepted

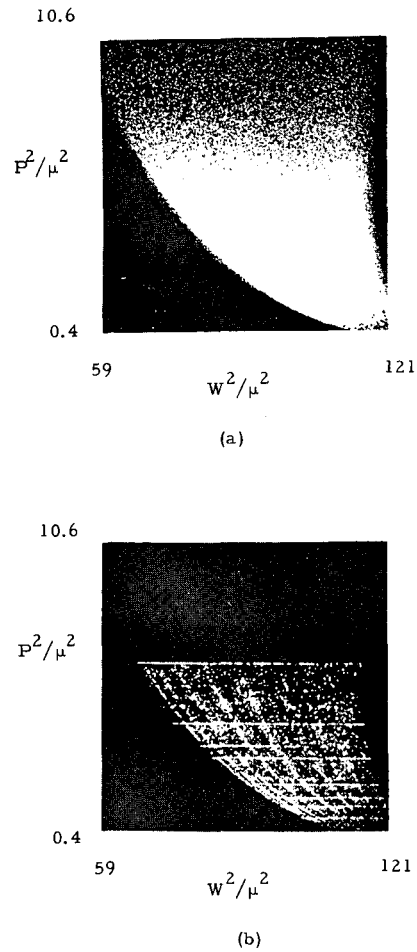

ZN-3652

Fig. 11. IBM 7090 CRT plot of 10^5 DRYLAB events: in (a) is shown the initial distribution in P^2 and W^2; in (b) is shown the search program values of the same variables.

the Bevatron events by means of the searched values of these variables should be attempted only with caution.

Another more instructive way to plot the DRYLAB events is in terms of scattering angles measured in the center-of-mass frame of the two nonspectator particles, θ^* and ϕ^* (see Appendix A). Figure 12 is such a CRT plot of the proton scattering angles. Here the events in which the search code has distinguished the pion from the proton have been plotted separately from those where the distinction could not be made. In this latter situation the angles corresponding to both choices have been plotted. Again a plot has been made in terms of the initial values and the search program fitted values of these variables. Since in DRYLAB a uniform distribution of events in the variables $\cos(\theta_1^*)$ and ϕ_1^* has been assumed, Fig. 12 represents, first, the selection process done by the apparatus on the uniform distributions, and, second the distortive effects of the search code on those selected. A number of observations were made.

(1) The ambiguous events in which the pion and the proton cannot be distinguished lie almost entirely in the backward region of θ_1^*. This is true no matter which assumption is made as to the particles' identity. From other such plots made as a function of time bin and theta zone of the recoil neutron, it was seen that the size of the region is not a strong function of the neutron's kinematics.

(2) The effects of the 4 deg beam exit hole are mostly confined to the forward regions of θ_1^*. However, as seen from other of these diagrams (not included in the text), the area subtended by this hole is a strong function of the neutron's kinematics. Losses resulting from high energy neutrons moving far forward in the laboratory system are small, amounting to less than 5% for neutrons in time bin 1 and theta zone 1. For slower neutrons emitted at larger laboratory polar angles this correction becomes much more serious; over 50% are lost for neutrons in time bin 7 and theta zone 7.

(3) The limited resolution of the detectors is once more evident in the lumping of events by the search code in Figs. 12c and 12d. This clustering of events appears much more serious in the variables ϕ_1^*

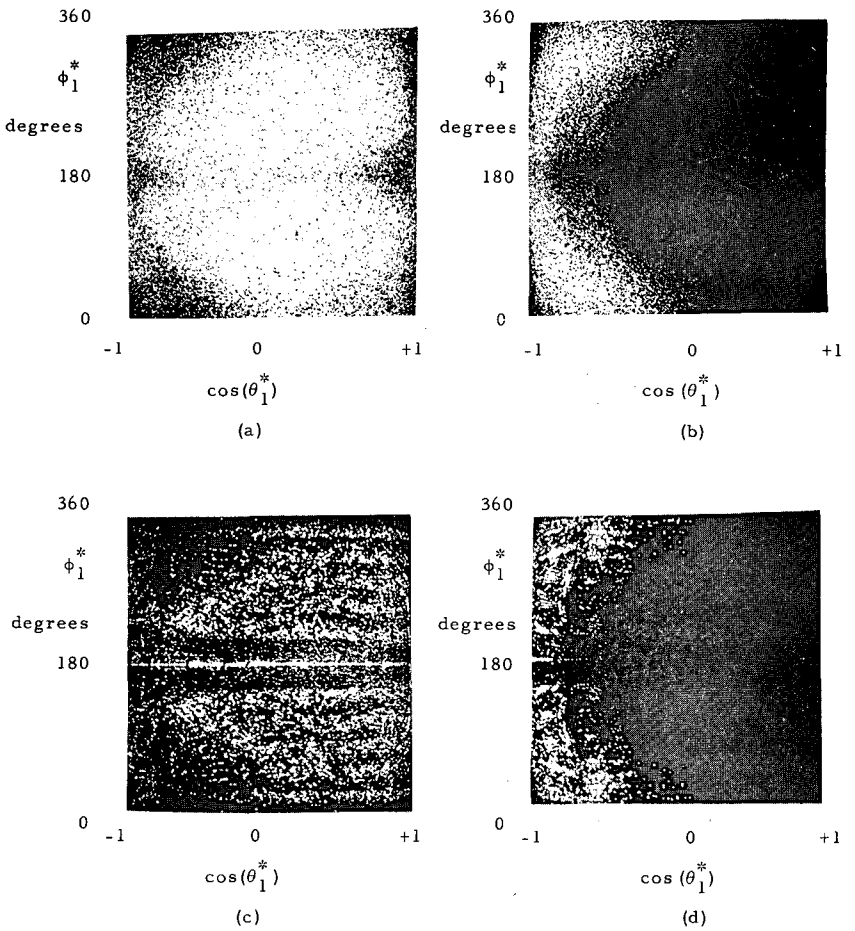

ZN-3653

Fig. 12. DRYLAB initial distribution for:
(a) pion and proton distinguishable,
(b) pion and proton not distinguishable;

DRYLAB final distribution for:
(c) pion and proton distinguishable,
(d) pion and proton not distinguishable, both solutions plotted.

than in θ_1^*, indicating that events might be sorted according to their searched values of this variable.

In view of the above observations it was decided to limit the analysis to events in which the proton and the pion could be distinguished and whose searched values of $\cos(\theta_1^*)$ were within the interval -0.5 to +0.5. This meant that the regions of the variables θ_1^* and ϕ_1^*, where the corrections for the counter geometry and for the search-code identification ambiguity were most serious, would not be included in the analysis. Although these restrictions reduced the number of events available for analysis by almost a factor of two, the reduction of the magnitude of the complex systematic corrections with the resulting increased confidence in the final analysis was felt worthwhile.

Tables IV and V, which list the events and give raw sections, include data from the entire range of θ_1^* and from both those events in which the nonspectator particles could be distinguished and those in which they could not. All of the subsequent data and discussion, unless specifically noted, will apply only to the sampling of events within the region

$$-0.5 < \cos(\theta_1^*) < +0.5$$

and in which the nonspectator particles can be distinguished. Note that although only Bevatron data in which the pion can be distinguished from the final-state proton will be included in the analysis, the comparison will be from a similar sampling of DRYLAB, and the cross sections so determined should be representative of the reaction as a whole.

C. Efficiency and Resolution of Detectors

1. Integrated Efficiencies

Since we are attempting to measure cross sections per unit P^2 and per unit W^2 interval, we must determine the sized bite in P^2, W^2 space each of our 49 data bins subtends. We must evaluate the integral

$$E_{ij} = \int E_{ij}\,(P^2, W^2)\, dP^2\, dW^2 ,$$

where $E_{ij}(P^2, W^2)$ denotes the detection efficiency for an event having a given P^2 and W^2 and whose associated neutron has given a count in the $\underline{i}$ th time bin and the $\underline{j}$ th theta zone. The quantity E_{ij} is the integrated efficiency for the data bin, the integration being carried out over all nonzero regions of $E_{ij}(P^2, W^2)$. This integration is not a simple one to perform since $E_{ij}(P^2, W^2)$ depends on quantities such as the detector geometry for both the neutrons and fast particles, incident beam size and momentum spectrum, the search-code efficiency, finite target size, as well as the neutron detection efficiency. If all of these effects were to be accounted for in the standard manner, tedious integrations would have to be performed over all of them as a function of $E_{ij}(P^2, W^2)$.

DRYLAB gives us a much simpler and more effective way of determining the 49 integrated efficiencies. The efficiency can also be written as

$$E_{ij}(P^2, W^2) = \frac{N'_{ij}(P^2, W^2)}{N_{ij}(P^2, W^2)} ,$$

where $N_{ij}(P^2, W^2)$ is the number of events incident on our apparatus per unit P^2 and W^2 interval, and $N'_{ij}(P^2, W^2)$ is the number of these events accepted as coming from the reaction under study, again per unit P^2 and W^2. We may also write our integral definition of E_{ij} as a summation:

$$E_{ij} = \sum \frac{N'_{ij}(P^2, W^2)}{N_{ij}(P^2, W^2)}\, \Delta P^2 \Delta W^2 .$$

Since our definition of $E_{ij}(P^2, W^2)$ should be independent of the incident distribution, $N_{ij}(P^2, W^2)$, we take it as a constant, N_0, which then

can be brought outside of the summation sign leaving

$$E_{ij} = \frac{1}{N_0} \sum N'_{ij}(P^2, W^2)\, \Delta P^2 \Delta W^2 .$$

The summation is now just the total number of events counted by the apparatus in the ij th data bin which we now write as C_{ij}; then, we have

$$E_{ij} = \frac{C_{ij}}{N_0} .$$

Now, E_{ij} can be easily evaluated from DRYLAB since N_0 is the total number of events tried divided by the P^2 and W^2 range from which the events were selected. We have

$$N_0 = 2706.4 \text{ per } (P^2/\mu^2)\ (W^2/\mu^2) .$$

We evaluate C_{ij} by noting the number of events which were accepted by the search code for each data bin. Since the analysis of the Bevatron data will be restricted to only the region of $\cos(\theta_1^*)$ between -0.5 and +0.5 and to events in which the nonspectator particles can be distinguished, similar restrictions were put on those sorted from the 10^5 DRYLAB events. We evaluated E_{ij} in this way for each of the 49 data bins. The factors by which the raw cross sections must be multiplied to give the cross sections per unit P^2 and W^2, $1/E_{ij}$, are given in Table VII.

This determination of E_{ij} includes the effects of the detector geometry on both the neutrons and the fast particles, the search code, the finite sized target, and the effects arising from all the other distributions built into DRYLAB.

2. Resolutions

Once more advantage was taken of DRYLAB to provide mean values and widths for each of the 49 data bins in the variables P^2 and

Table VII. Inverse integrated efficiency: $1/E_{ij}$ in μ^2/P^2 μ^2/W^2.

Time bin	θ Zone						
	1	2	3	4	5	6	7
1	2.74	1.35	0.91	0.72	0.60	0.54	0.48
2	5.52	3.07	2.05	1.67	1.38	1.18	1.11
3	10.25	4.93	3.33	2.56	1.91	2.02	2.04
4	24.16	7.98	4.76	4.41	3.65	3.62	5.97
5	21.48	10.10	6.68	5.42	4.30	6.11	6.94
6	23.13	9.88	8.96	7.27	6.32	7.64	9.14
7	50.12	25.53	21.48	16.71	18.54	20.82	38.66

W^2. The magnetic tape containing the 10^5 DRYLAB events was sorted and for each of the 49 data bins the mean values of P^2 and W^2 were computed from the initial P^2 and W^2 values of events in the bin using

$$\overline{P}^2 = \frac{1}{N}\sum_k P_k^2 ,$$

and

$$\overline{W}^2 = \frac{1}{N}\sum_k W_k^2$$

for each data bin. Then, $\overline{P}_{ij}^2$ and $\overline{W}_{ij}^2$ are the mean values of P^2 and W^2 for the ij th bin, P_k^2 and W_k^2 are the initial values of P^2 and W^2 for an event with $\cos(\theta_1^*)$ between -0.5 and +0.5 and with distinguishable nonspectator particles, and N is the total number of such events in that data bin. The rms widths of the bins in terms of these variables $\overline{\Delta P}_{ij}^2$ and $\overline{\Delta W}_{ij}^2$ were computed using

$$\Delta P^2 = \frac{1}{N}\sqrt{\sum_k (P^2 - P_k^2)^2} ,$$

and

$$\Delta W^2 = \frac{1}{N}\sqrt{\sum_k (W^2 - W_k^2)^2}$$

for each data bin. By using the initial values of P^2 and W^2 rather than those found by the search code, any systematic tendency of the code to shift these values could be taken into account. Tables VIII and IX summarize the results.

Tables VIII shows that the mean values of P^2 and their widths now become dependent on the theta zone of the neutron as well as the time bin. This arises because the other resolutions of the apparatus, especially the number of fast particles lost through the 4 deg beam exit hole, have a P^2 dependence as well as a dependence on the neutron

Table VIII. Mean values of P^2/μ^2 and rms widths from DRYLAB.

Time Bin	θ Zone 1	2	3	4	5	6	7
1	5.35 ± 1.35	5.38 ± 1.41	5.41 ± 1.44	5.37 ± 1.46	5.32 ± 1.44	5.32 ± 1.40	5.39 ± 1.40
2	3.69 ± 1.10	3.71 ± 1.10	3.74 ± 1.11	3.72 ± 1.13	3.76 ± 1.14	3.68 ± 1.08	3.80 ± 1.10
3	2.90 ± 1.09	2.89 ± 1.07	2.90 ± 1.06	2.94 ± 1.15	2.93 ± 1.10	2.96 ± 1.14	3.15 ± 1.18
4	2.10 ± 0.59	2.19 ± 0.80	2.18 ± 0.78	2.29 ± 0.83	2.32 ± 0.85	2.32 ± 0.84	2.61 ± 0.92
5	1.58 ± 0.57	1.84 ± 0.73	1.82 ± 0.70	1.78 ± 0.65	1.87 ± 0.71	1.85 ± 0.72	2.14 ± 0.75
6	1.43 ± 0.58	1.42 ± 0.58	1.45 ± 0.64	1.49 ± 0.65	1.57 ± 0.69	1.60 ± 0.70	1.82 ± 0.75
7	1.06 ± 0.38	1.15 ± 0.45	1.19 ± 0.53	1.16 ± 0.44	1.23 ± 0.52	1.36 ± 0.43	1.58 ± 0.42

Table IX. Mean values of W^2/μ^2 and rms widths from DRYLAB.

Time Bin	θ Zone 1	2	3	4	5	6	7
1	106.5 ± 5.5	104.2 ± 5.4	100.4 ± 5.1	94.7 ± 4.7	87.8 ± 4.0	79.8 ± 3.4	70.8 ± 3.1
2	98.5 ± 5.9	96.6 ± 5.6	93.5 ± 5.2	88.9 ± 4.8	83.3 ± 4.1	76.5 ± 3.4	69.2 ± 2.8
3	93.4 ± 6.7	91.6 ± 6.4	88.8 ± 5.8	85.0 ± 5.6	80.0 ± 4.5	74.2 ± 3.8	68.1 ± 3.1
4	87.9 ± 4.7	86.7 ± 5.8	84.1 ± 5.3	81.5 ± 5.1	77.2 ± 4.5	72.1 ± 3.6	67.2 ± 2.8
5	82.6 ± 5.5	83.7 ± 6.2	81.2 ± 5.7	78.1 ± 4.8	74.6 ± 4.5	70.0 ± 3.7	65.8 ± 2.7
6	80.9 ± 5.7	79.7 ± 5.6	77.8 ± 5.5	75.5 ± 5.1	72.4 ± 4.6	68.4 ± 3.6	64.5 ± 2.6
7	76.7 ± 5.0	76.6 ± 5.3	75.2 ± 5.6	72.6 ± 4.4	69.9 ± 4.4	67.1 ± 3.0	63.7 ± 2.1

angle. Again, these tables reflect the effects of all the distributions incorporated into DRYLAB. The quantities listed in Tables VII to IX were also computed by integrating in the usual way over the initial distributions making some simplifying assumptions as to the geometry. These results agreed very well with those of DRYLAB for data bins where the effects of the 4 deg hole and the target and beam size should not exert large effects. In the other regions, the deviations were in the expected directions.

3. Scattering Corrections Applied

Only corrections due to events lost by the scattering of neutrons in the hydrogen target and due to the scattering of fast charged particles in the thick scintillation detectors (discussed at the end of Sec. V-A) remain to be applied. Both of these could have been incorporated into DRYLAB but since adequate means of dealing with them already had been developed, the additional complexity which would have been required of DRYLAB was not thought necessary. As both of these are discussed in detail by Johnson,[4] only a cursory discussion of the principles involved and the assumptions made along with the magnitude of the effects are given.

The larger of these corrections involves events which would have been lost because one of the final-state charged particles interacted with a nucleus in the scintillation detector resulting in one or more particles which triggered an adjacent counter. The effects of the 0.6 cm of lead covering the detector or of the other constituents of the detector are negligible compared to the effects of the carbon nuclei contained in the scintillation material. Monte Carlo calculations were done with a number of reasonable assumptions as to the form of the interaction, and the particle trajectories were followed through the scintillator. A tally was kept of those which would have triggered adjacent counters. The fraction which would have given such spurious events was found only weakly dependent on the hypotheses made and a representative average scattering probability, s(m), was made for each zone, m. The magnitude of s(m) varied from 13.8% for the first theta zone to

11.3% for the seventh. Each event was then weighted according to the expression

$$\frac{1}{1 - s(j)} \quad \frac{1}{1 - s(k)}$$

where j and k are the theta zones which the two fast particles entered. This correction is included in the subsequent data.

A Monte Carlo computation was also performed to determine the effects of neutron scattering within the hydrogen target. The trajectories of representative events were followed through the target and their probability for scattering was calculated from the known neutron-proton cross sections. When a scattering occurred, the neutron -- with its energy now properly reduced because of the scattering -- was followed as it entered the detector array. The known probability for detection was invoked as it entered the scintillator and, if counted, the event was transferred to the search code where an attempt was made to fit it to the kinematics of our reaction. From a study of such events, an estimate of how scattering in the liquid hydrogen target effected the final distributions could be made and the data appropriately corrected. Such a correction amounted to at most a 10% effect for any data bin and has been included in the subsequent analysis.

VI. RESULTS, DISCUSSION, AND CONCLUSION

A. Primary Data

Table X and Fig. 13 show the double distribution, $\frac{\partial^2\sigma}{\partial P^2 \partial W^2}$, for each of the seven time bins. These data included the subtractions from the four target-delay conditions and all the corrections mentioned in the preceding section. Table X and Fig. 13 represent only the data between the limits of the center-of-mass scattering variable, $\cos(\theta_1^*)$, defined in Appendix A, of -0.5 and +0.5.

B. Analysis of the data in W^2

With the experimental data plotted in Fig. 13 is also plotted the peripheral model predictions of Selleri.[26] The curve was drawn by using formula I-4 and by inserting for the total cross sections the cross sections appropriate to our center-of-mass angular interval,

$$\sigma(W) = 2\pi \int_{-0.5}^{+0.5} \frac{d\sigma(W)}{d\Omega}\, d(\cos\theta^*),$$

where $\frac{d\sigma(W)}{d\Omega}$ is the differential scattering cross section for positive pions on protons at a pion center-of-mass angle of θ^* and a total center-of-mass energy given by W. A literature survey, the findings of which are presented in Appendix C, was made to codify existing data on pion-proton angular distributions. In all subsequent comparisons with this peripheral model formula, the above restricted cross section will be used.

To aid in comparing the distributions in the variable W^2/μ^2 with the physical pion-proton cross sections, whose salient features are most familiar when discussed in terms of the incident-pion laboratory kinetic energy, Fig. 14 is a graph showing the relation of the two variables.

Table X. Measured cross sections, $\frac{\partial^2 \sigma}{\partial \frac{P^2}{\mu^2} \partial \frac{W^2}{\mu^2}}$, and errors in μb.

Time Bin	θ Zone 1 (μb)	2 (μb)	3 (μb)	4 (μb)	5 (μb)	6 (μb)	7 (μb)
1	4.22 ± 0.78	3.12 ± 0.48	3.04 ± 0.41	3.08 ± 0.35	3.53 ± 0.35	4.79 ± 0.36	2.39 ± 0.26
2	6.96 ± 1.38	6.21 ± 0.88	5.63 ± 0.73	6.94 ± 0.76	9.42 ± 0.81	10.35 ± 0.80	3.93 ± 0.42
3	9.18 ± 2.03	8.44 ± 1.19	9.22 ± 0.97	11.72 ± 1.09	11.65 ± 1.01	9.35 ± 0.91	4.43 ± 0.56
4	22.49 ± 6.14	14.54 ± 2.28	19.25 ± 1.63	18.86 ± 1.65	17.62 ± 1.34	9.42 ± 1.28	8.87 ± 1.62
5	23.33 ± 5.48	14.32 ± 2.66	16.64 ± 1.90	16.19 ± 1.74	11.19 ± 1.40	11.09 ± 1.62	4.62 ± 1.51
6	21.42 ± 6.03	18.47 ± 2.92	22.48 ± 2.95	17.11 ± 2.50	12.27 ± 1.94	10.14 ± 1.79	5.01 ± 2.04
7	22.90 ± 12.18	18.61 ± 5.95	20.79 ± 5.71	11.61 ± 4.71	16.70 ± 4.20	7.33 ± 3.96	− 1.58 ± 7.50

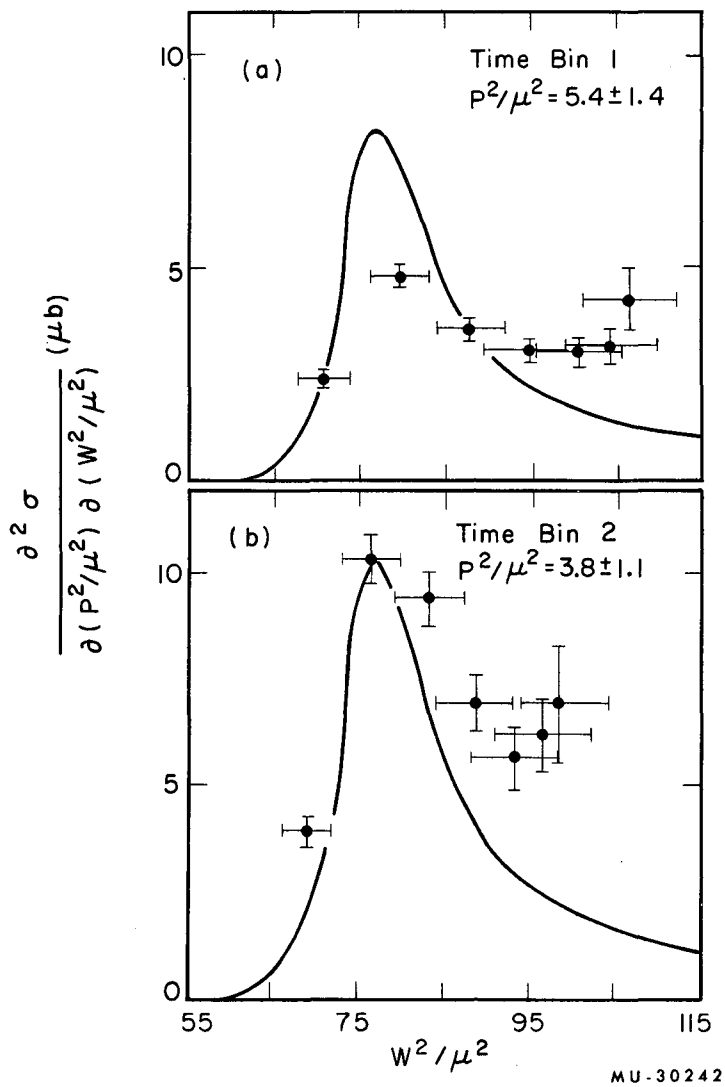

Fig. 13. Double distribution $\frac{\partial^2 \sigma}{\partial(P^2/\mu^2)\partial(W^2/\mu^2)}$ for the seven time bins.

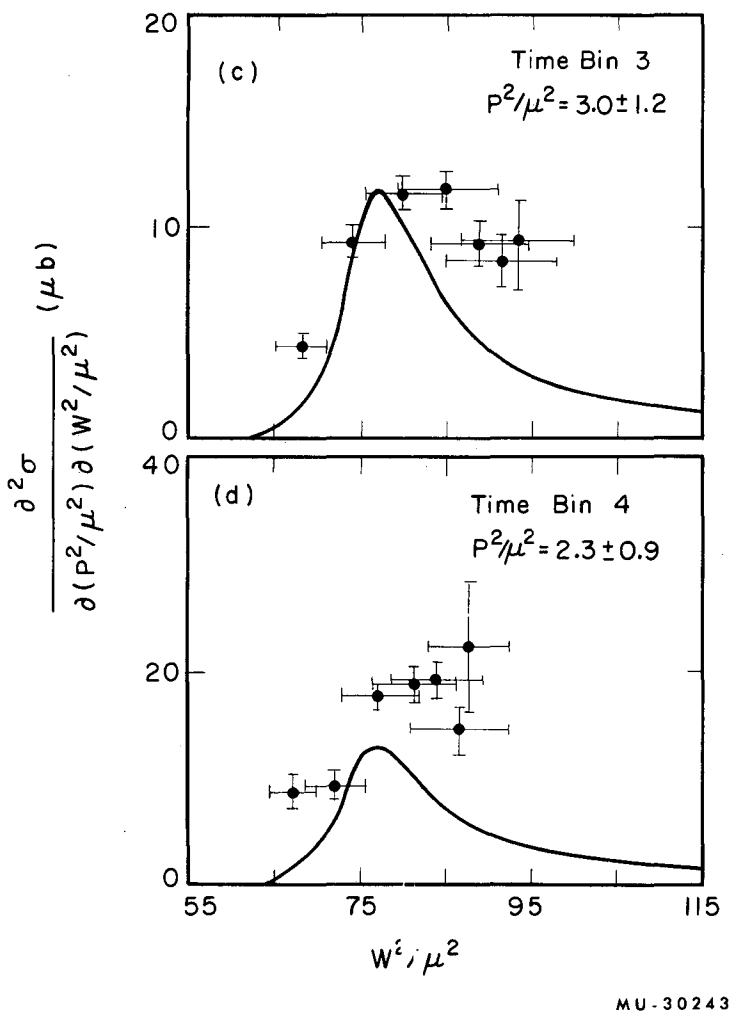
(c)
Time Bin 3
$P^2/\mu^2 = 3.0 \pm 1.2$
(d)
Time Bin 4
$P^2/\mu^2 = 2.3 \pm 0.9$
$\frac{\partial^2\sigma}{\partial(P^2/\mu^2)\,\partial(W^2/\mu^2)}$ (μb)
W^2/μ^2
20
10
0
40
20
0
55
75
95
115
MU-30243

Fig. 13 (Cont.)

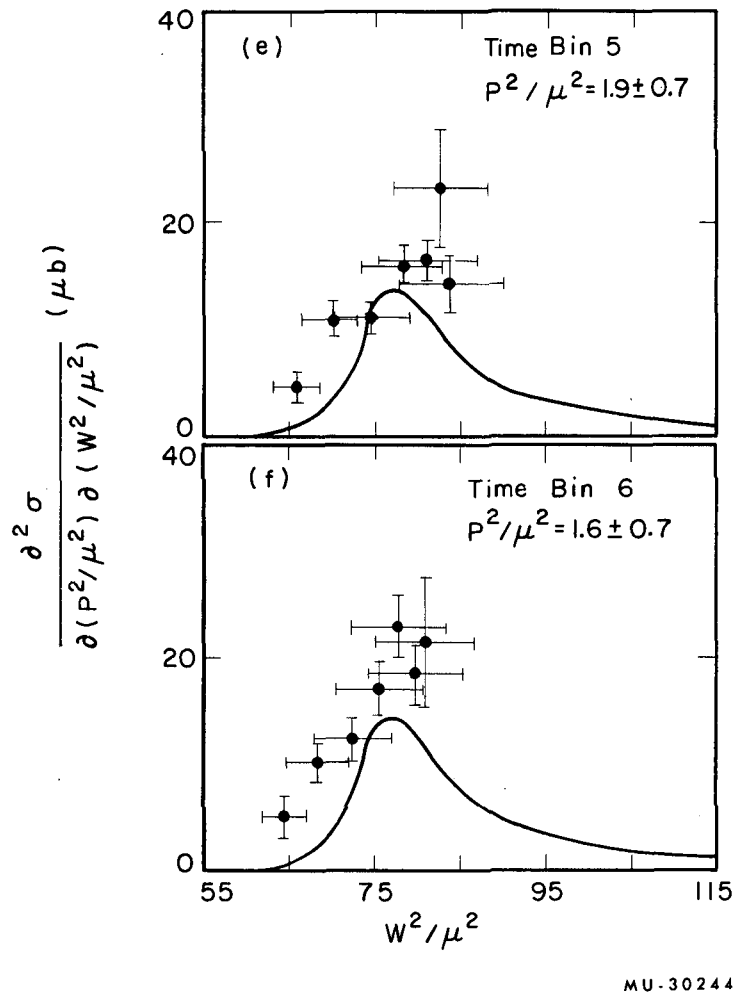
(e)
Time Bin 5
$P^2/\mu^2 = 1.9 \pm 0.7$
(f)
Time Bin 6
$P^2/\mu^2 = 1.6 \pm 0.7$
$\frac{\partial^2 \sigma}{\partial (P^2/\mu^2)\, \partial (W^2/\mu^2)}$ (μb)
W^2/μ^2
0
20
40
55
75
95
115
MU-30244

Fig. 13 (Cont.)

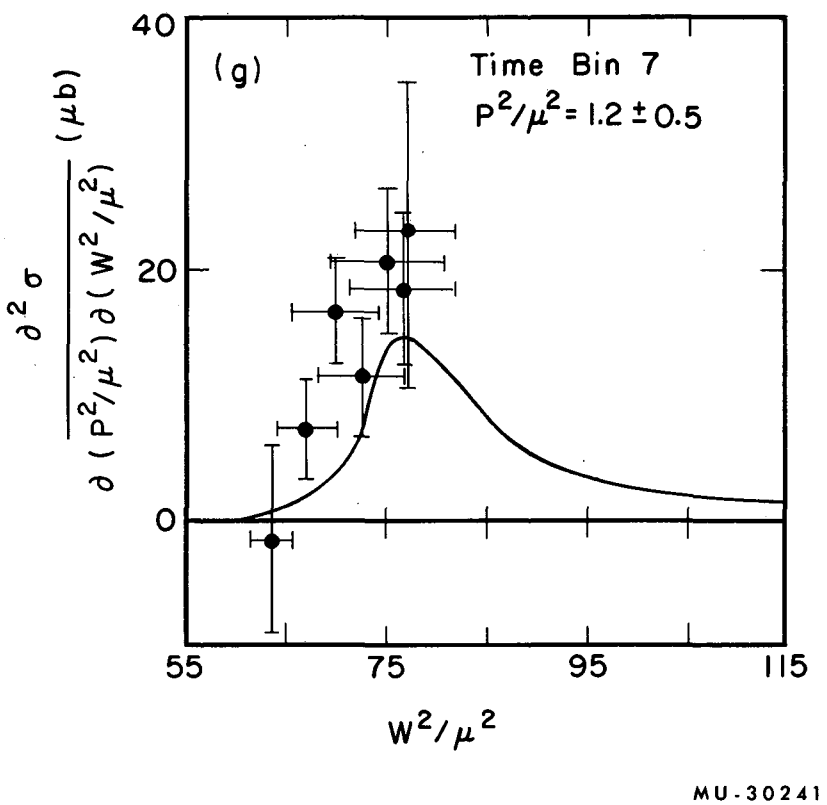
(g)
Time Bin 7
$P^2/\mu^2 = 1.2 \pm 0.5$
40
20
0
55
75
95
115
W^2/μ^2
$\frac{\partial^2 \sigma}{\partial (P^2/\mu^2)\, \partial (W^2/\mu^2)}$ (μb)
MU-30241

Fig. 13 (Cont.)

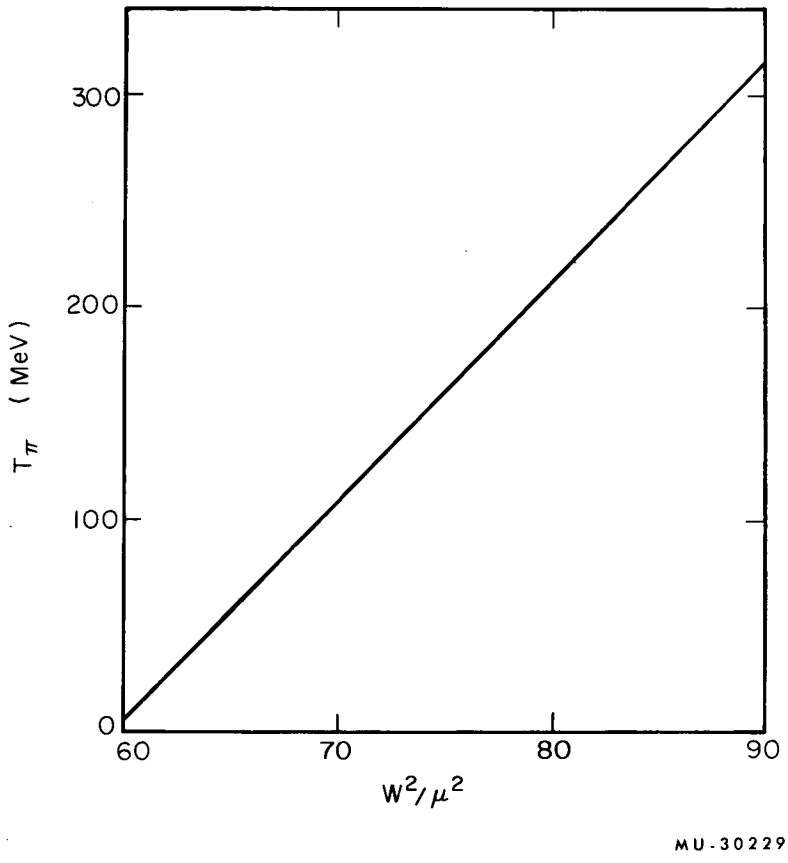

Fig. 14. Kinematical relation between T_π, pion laboratory kinetic energy, and W^2/μ^2, total center-of-mass energy squared for pion-proton collisions.

The most striking feature of the data presented in Fig. 13 is the enhancement of the cross section in the region of the 3/2-3/2 pion-nucleon resonance occurring at a value of $W^2/\mu^2 = 78.3$. The second apparent rise of the cross section at the high W^2 ends of bins 1 and 2, while of dubious statistical significance, also represents data from neutron counters immediately bordering the incident proton beam and which had the largest background subtractions.

To investigate the overall structure of the data in the variable W^2, an integration of the cross section was made over the variable P^2. In order that a comparison could be made with a similar kinematical region of the peripheral model and phase space, the integration was restricted to neutron energy limits of 10 to 55 MeV and polar angular limits of 4 to 60 deg — — roughly the region seen by the detectors — — and the same limits used for all three cases. Figure 15 shows the results of the integration. The upper curve is derived from the peripheral model and the lower curve represents invariant phase space normalized to a total cross section of 10 mb for the full kinematical neutron limits of the reaction. The excellent agreement of the peripheral model for the cross section near the peak of the resonance must be considered fortuitous since the cross sections for individual time bins show much larger deviations but in directions which cancel when summed. Still, except for a somewhat larger width, the peripheral model agrees well with the position and general shape of the resonance in the variable W^2. Phase space gives an estimate of the cross section too low by at least an order of magnitude.

It is of interest to compare this data with the recent work of Chadwick et al.[27] in which the high-energy inelastic-proton spectra resulting from proton-proton collisions was studied. Their data at an incident proton energy of 1.35 and 2.1 BeV (equivalent to an incident momentum of 2.09 and 2.89 BeV/c) bracket our results at 2.5 BeV/c incident proton momentum. Quantitative comparisons are difficult since Chadwick et al. detected only the final-state proton, which could have resulted from either of the reactions

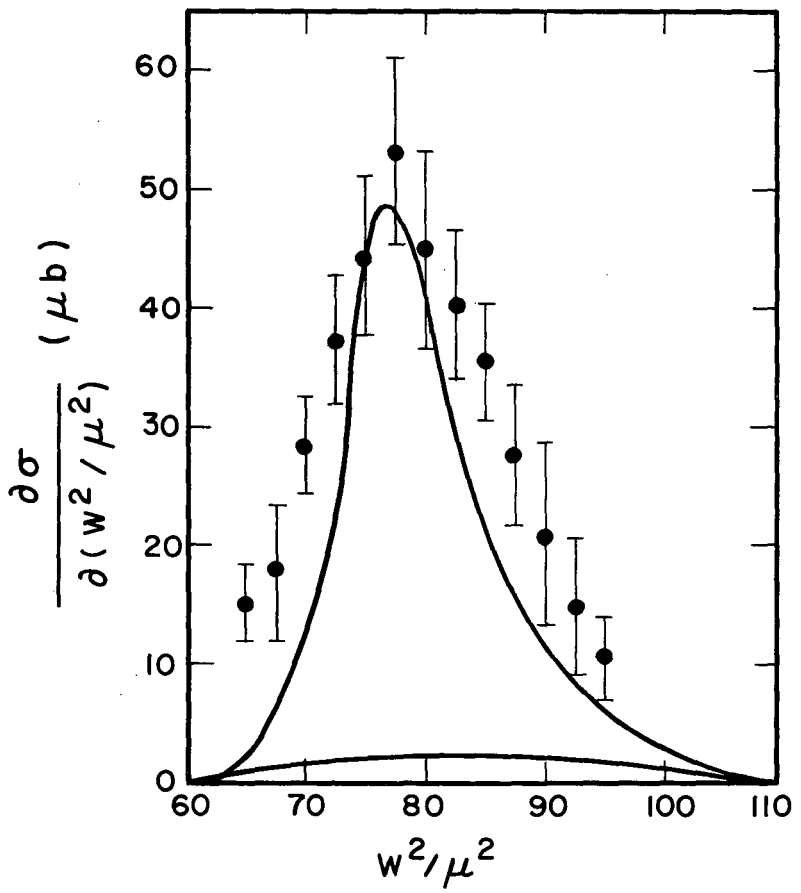

MU-30230

Fig. 15. Differential cross section $\partial\sigma / \partial \frac{W^2}{\mu^2}$ for neutron energies between 10 and 55 MeV and polar angles between 4 and 60 deg. The upper curve is the predicted cross section of the peripheral model, the lower is phase space.

$$p + p \rightarrow p + p + \pi^0$$

$$\rightarrow p + n + \pi^+,$$

and, in their peripheral model comparison, they have assumed an isotropic decay of the 3/2-3/2 isobar. However a number of qualitative comparisons can be made in the region of the resonance by examining graphs of their proton distributions plotted on page 1828 of their text. They find good agreement with the peripheral model at low momentum transfers whereas our data tend to give cross sections which are high. If the isobar decays isotropically as Chadwick assumes in his comparison, then the calculated peripheral model curves shown with our data should be multiplied by a factor of about 1.6 in the region of the resonance since we have assumed a differential cross section proportional to approximately $1 + 3 \cos^2(\theta^*)$ in this region. This would place our data at low momentum transfer in reasonably good agreement with the peripheral model, although with this extra factor of 1.6, our agreement would be even worse at higher momentum transfer points. The data of Chadwick et al. also exhibit cross sections which fall short of the peripheral model at high momentum transfers, although our deviations appear greater.

C. Analysis of the data in P^2

For each of the seven time bins the measured distribution was fitted by a polynomial series in the variable W^2. A plot could then be made at a given value of W^2, as a function of P^2, using data from each of the time bins. Figure 16 shows plots of the P^2 distribution for three values of W^2. Values of W^2/μ^2 were chosen equal to 70.0, 78.3, and 85.0, corresponding to physical pion-proton center-of-mass energies at pion laboratory kinetic energies of 110, 195, and 265 MeV. On the same figures are the peripheral model predictions. At W^2/μ^2 equal to 85.0, only time bins 3-7 contribute because of the kinematical limitations of the detection apparatus (see Fig. 3).

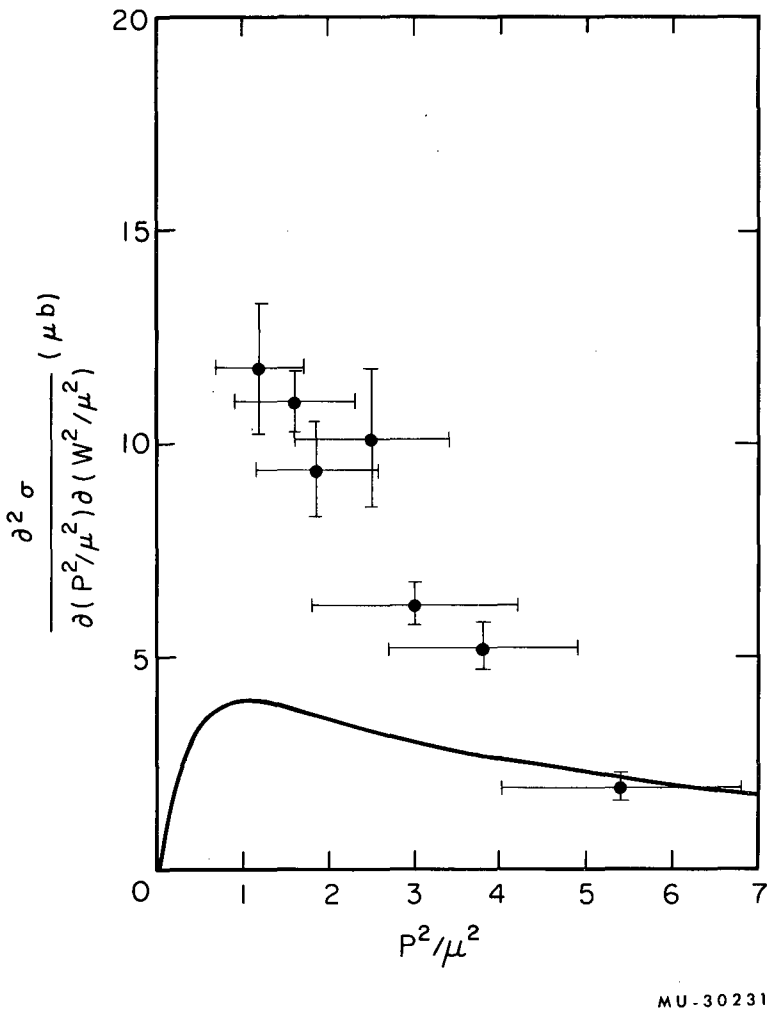

Fig. 16a. Measured partial cross section as a function of P^2/μ^2 for $W^2/\mu^2 = 70$.

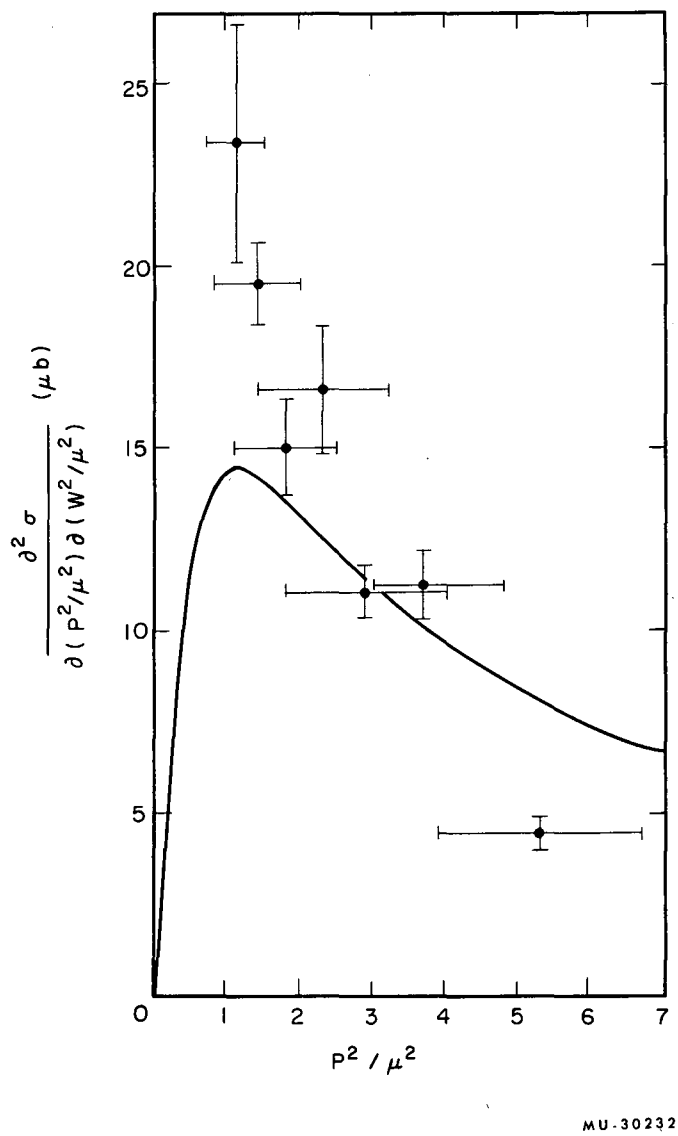

Fig. 16b. Measured partial cross section as a function of P^2/μ^2 for $W^2/\mu^2 = 78.3$.

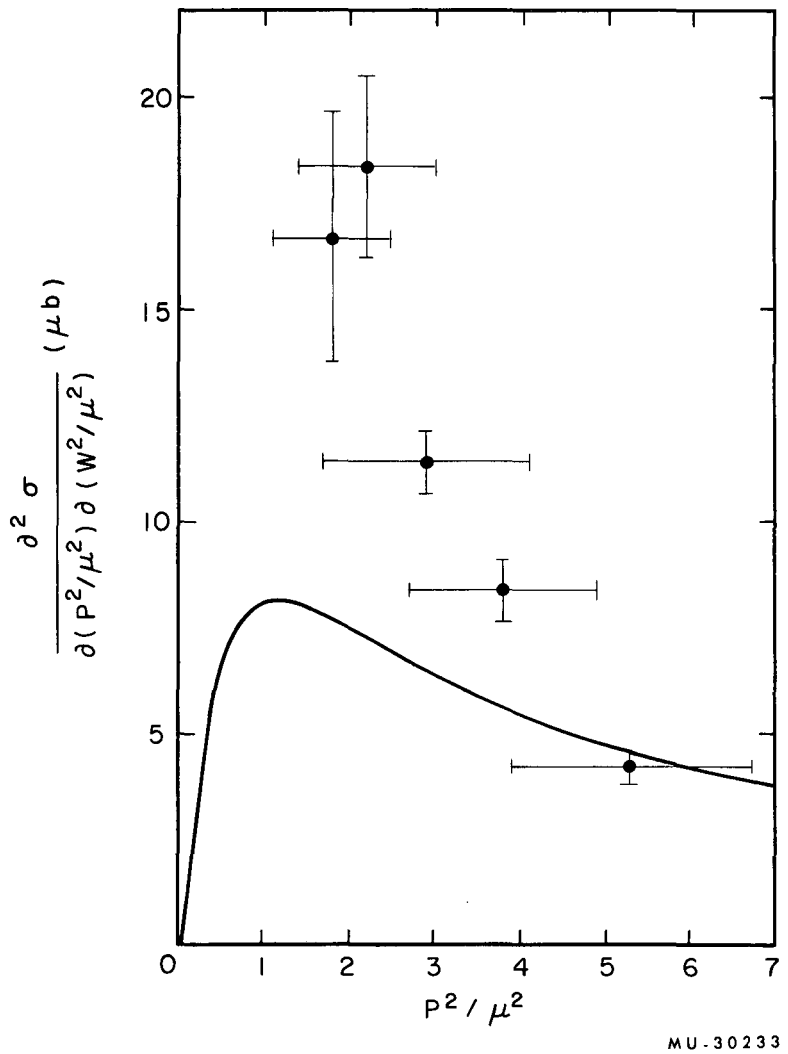

Fig. 16c. Measured partial cross section as a function of P^2/μ^2 for $W^2/\mu^2 = 85$.

Agreement with the peripheral model is poor. Even if one were to assume an angular distribution in the variable $\cos(\theta^*)$ different from the peripheral model predictions, this would only result in a constant multiplicative factor for each graph of Fig. 16. The assumption of isotropy would increase the drawn peripheral model curve by a factor of about 1.6 for Fig. 16b and a somewhat smaller factor for the other two. There would still be a marked discrepancy in the P^2 dependence of these cross sections from that of the peripheral model predictions.

An attempt was made to apply the Chew-Low extrapolation scheme to the calculation of the known pion-proton cross section from the measured distributions in P^2 and W^2. For each of the 49 data bins the Chew-Low extrapolation function, F [defined in Eq. (I-1)] was computed. Once more DRYLAB was employed to compute a properly weighted coefficient of the cross section term occurring in F. Table XI is a list of the values of F with the corresponding rms errors for each bin. The data for each time bin was fitted by a polynomial expansion in W^2. Using data from each of the bins a plot could then be made as a function of P^2, for a particular W^2. Again three values were chosen, W^2/μ^2 equal to 70.0, 78.3, and 85.0, corresponding to physical pion-proton center-of-mass energies at incident pion laboratory kinetic energies of 110, 195, and 265 MeV. Figure 17 is a plot of the results. At a value of $P^2/\mu^2 \approx -1$, the position of the pole due to the single pion exchange, our extrapolated value of F should be equal to the negative of the pion-proton cross section at a total center-of-mass energy given by W, [Eq. (I-2)]. Note that since our data is only from the region $-0.5 < \cos(\theta^*) < +0.5$, our extrapolated cross section should also correspond to a similar region given by

$$\sigma(W) = 2\pi \int_{-0.5}^{+0.5} \frac{d\sigma}{d\Omega}\, d[\cos(\theta^*)]$$

where $\frac{d\sigma}{d\Omega}$ is the differential cross section for the elastic scattering of positive pions on protons at a total center-of-mass energy given by W. From the tabulation of Appendix C, $\sigma(W)$ was calculated for each of the three plots and its position is shown at $P^2/\mu^2 = -1$.

Table XI. Chew-Low extrapolation function, F, with rms errors in mb.

Time Bin	θ Zone 1 (μb)	2 (μb)	3 (μb)	4 (μb)	5 (μb)	6 (μb)	7 (μb)
1	73.5 ± 13.6	57.4 ± 8.8	60.9 ± 8.2	68.6 ± 7.8	92.1 ± 9.2	161.4 ± 12.1	127.2 ± 13.9
2	77.1 ± 15.2	72.0 ± 10.2	71.0 ± 9.2	97.6 ± 10.7	158.2 ± 13.6	215.4 ± 16.6	128.7 ± 13.8
3	78.8 ± 17.4	75.2 ± 10.6	88.5 ± 9.3	128.2 ± 11.9	149.2 ± 13.0	154.1 ± 14.9	116.9 ± 14.8
4	139.0 ± 37.9	98.2 ± 15.4	138.9 ± 11.8	159.1 ± 13.9	176.6 ± 13.5	119.9 ± 16.2	188.6 ± 34.4
5	115.3 ± 27.1	83.5 ± 15.5	103.4 ± 11.8	109.8 ± 11.8	93.5 ± 11.7	117.4 ± 17.2	85.6 ± 28.0
6	99.3 ± 28.0	89.2 ± 14.1	121.4 ± 15.7	103.5 ± 15.1	91.2 ± 14.4	99.8 ± 17.6	86.7 ± 35.3
7	89.8 ± 47.8	79.9 ± 25.5	98.7 ± 27.1	60.5 ± 24.6	109.1 ± 27.5	66.0 ± 35.6	− 25.7 ± 121.6

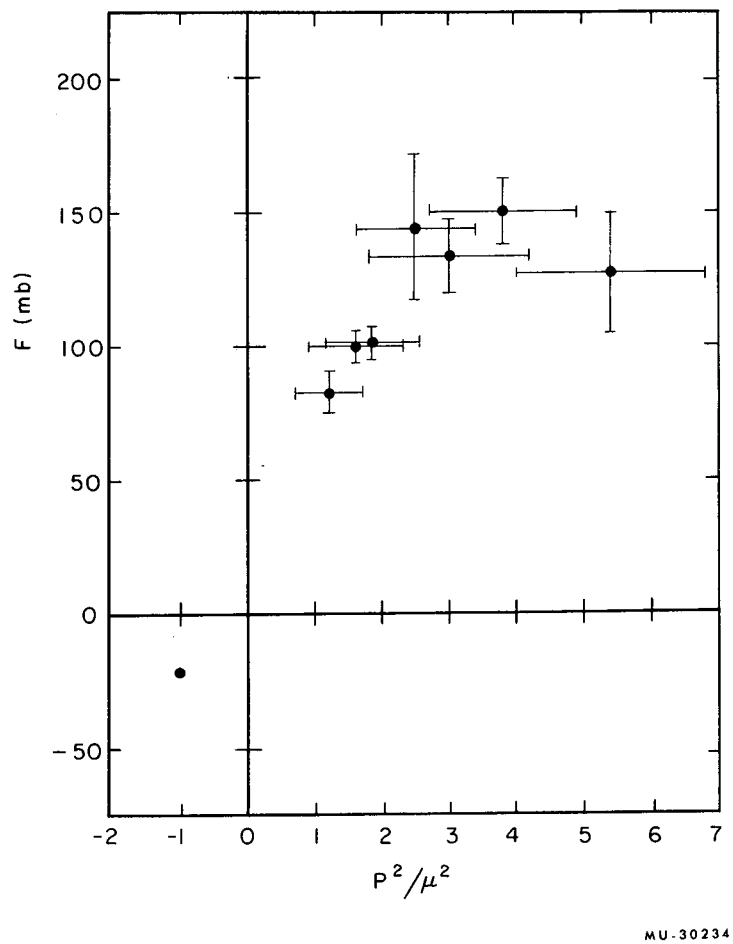

Fig. 17a. Chew-Low extrapolation plot for $W^2/\mu^2 = 70.0$.

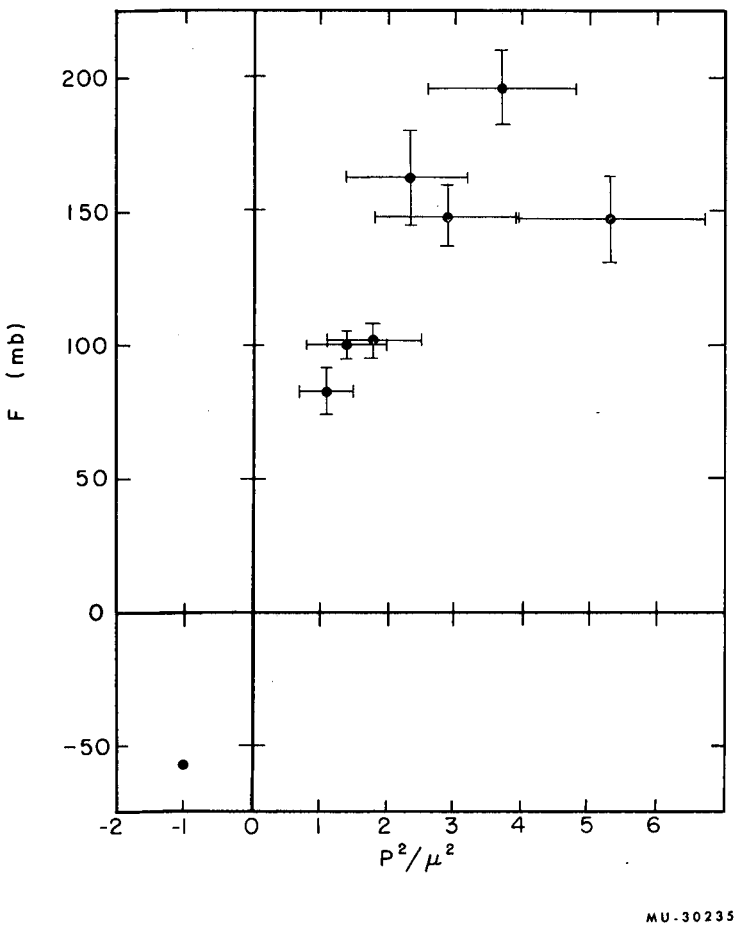

Fig. 17b. Chew-Low extrapolation plot for $W^2/\mu^2 = 78.3$.

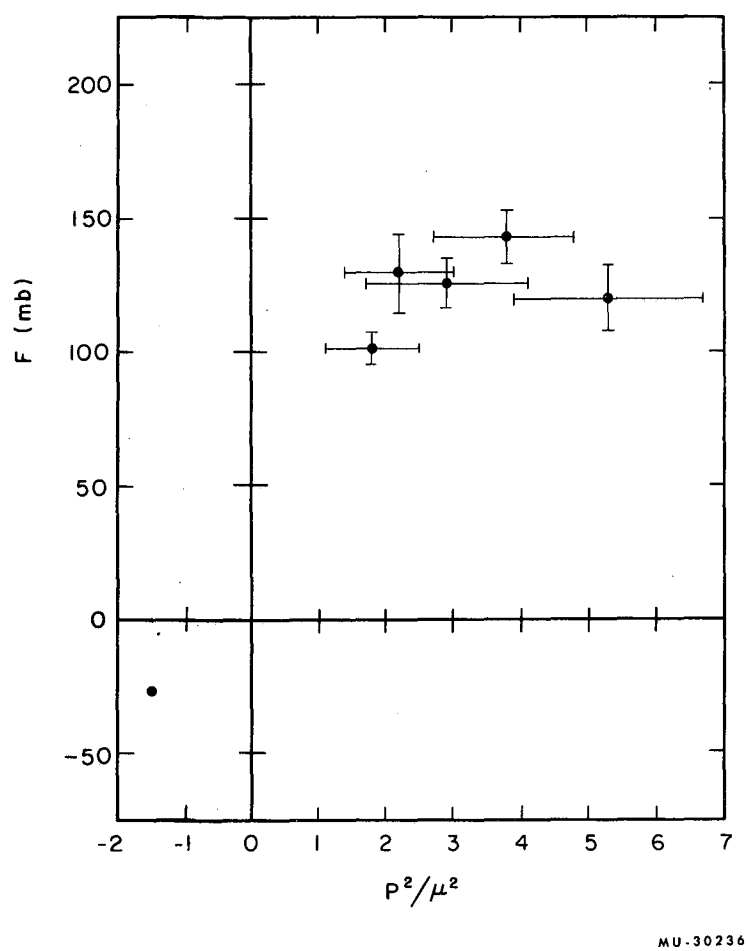

Fig. 17c. Chew-Low extrapolation plot for $W^2/\mu^2 = 85.0$.

For each of the three plots, the extrapolation procedure seems to fail in the sense that no straight line can be drawn through all the data which will give the correct value for the pion-proton cross section. The data near the resonance (Fig. 17b) comes closest to fitting a reasonable linear extrapolation if momentum transfers less than $4\mu^2$ only are used; data above and below the resonance show discrepencies even at these momentum transfers.

Two other experiments have been done at somewhat different incident energies to study the Chew-Low extrapolation procedure for the same reaction. One was an experiment by Smith et al.[28] at an incident proton energy of 2.85 BeV and the other by Fickinger et al.[29] at 2.0 BeV. Both experiments used a liquid hydrogen bubble chamber. In the analysis of their low momentum transfer data, they had considered an event to contribute to the cross section at a particular range of momentum transfer if the event could have corresponded to <u>either</u> a small momentum transfer to the target proton (hence a low energy neutron in the laboratory system) or to a small momentum transfer to the projectile (hence a high energy neutron in the laboratory system). This is valid since the target and projectile are identical particles; however, if the cross section is so measured, then in the application of the Chew-Low extrapolation formula,[3] it must be divided by two. This was not done in these two papers[30] and hence the extrapolation plots published in them are in error. Figure 18 shows the corrected plots, near the peak of the resonance, from these two experiments with the data from this work. Our data have been multiplied by a factor of three since our center-of-mass range is limited from $\cos(\theta^*)$ equal to 0.5 to -0.5. The factor of three assumes a distribution of $\cos(\theta^*)$ of the form $1 + 2.5 \cos(\theta^*)$ as reported by Fickinger et al.[31] for this reaction at 2.0 BeV. However, the data of Smith et al.[28] at 2.85 BeV indicate isotropy. Agreement seems reasonably good whichever of these assumptions is made.

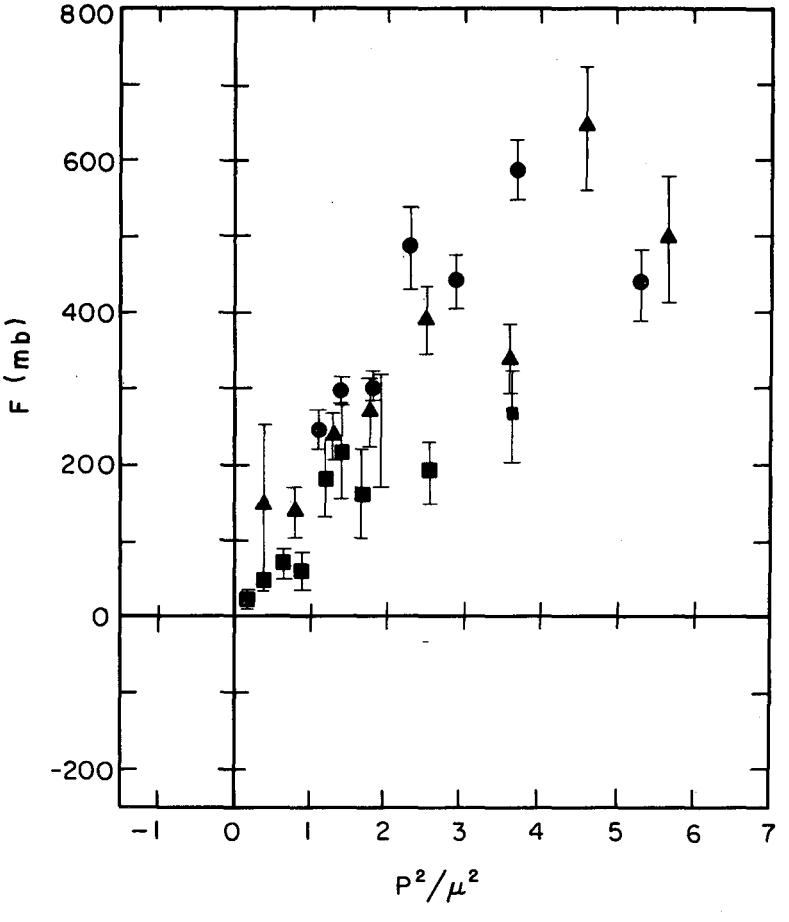

MU-30237

Fig. 18. Comparison of the Chew-Low extrapolation plot from this experiment and the corrected plots from other experiments near the 3/2-3/2 resonance. The data shown from this experiment is that from Fig. 17b multiplied by a factor of three.

⊙	1.73 BeV	this experiment
△	2.00 BeV	Fickinger et al.
□	2.85 BeV	Smith et al.

VII. CONCLUSIONS

Our data in the region of P^2/μ^2 between 1.1 and 5.4 show strong deviations from a linear fit using the Chew-Low extrapolation formula to obtain the known pion-proton cross sections. When compared with other experiments, our extrapolation plot near the peak of the 3/2, 3/2 resonance appears in good agreement with them.

The peripheral model predictions of Selleri[26] agree well with the observed position and reasonably well with the observed shape of the 3/2, 3/2 resonance if an integration is made over P^2. However, the dependence of the cross section on P^2 is not in agreement in the region of the resonance, the predictions being too small at high P^2 and too large at low P^2.

ACKNOWLEDGMENTS

I thank my colleagues in this experiment, Professor Thomas Ypsilantis, Dr. Clyde Wiegand, Dr. William B. Johnson, Dr. Tom Elioff, and Dr. Leonard B. Auerbach. It is only through their combined efforts that this experiment was made possible. More specifically, Dr. Wiegand's contribution to the very involved electronics and his dogged insistence on methodical procedures were crucial to the experiment's success. Without Professor Ypsilantis' initial stimulation and his continued and determined optimism in the face of the many set backs during the three Bevatron runs the experiment could not have been performed. The interest and encouragement of my research director Professor Emilio Segrè during all phases of the experiment was also greatly appreciated.

Many groups at the Lawrence Radiation Laboratory contributed materially to the success of this experiment and all their efforts are herein acknowledged. In particular Mr. Quentin Kerns, Mr. Fred Kirsten, Mr. Dick Mack, Mr. Stanley Baker, Mr. Thomas Nunamaker, and Mr. Arthur Bjerke were instrumental in the design and construction of the electronic circuitry used in this experiment. Mr. Cedric Larson's design of the neutron counter supports deserved commendation. The operating crews of both the Bevatron and the 184 inch cyclotron deserve mention for their aid in setting up the experiment and their excellent operation of these accelerators during the runs. The aid of the computing group, and specifically Mr. Joe Good for his many contributions to the writing of the computer codes and Mr. Jerry Borges for expediting many calculations, is appreciatively acknowledged. Finally, Professor Geoffrey Chew's interest and encouragement in this experiment through many discussions is also gratefully acknowledged.

This work was done under the auspices of the U. S. Atomic Energy Commission.

APPENDICES

A. Summary of Three-Body Kinematics

1. Nomenclature

In describing the reaction

$$M_1 + M_2 \rightarrow M_3 + M_1 + \mu$$

we will use the Roman letter M to represent a particle with a nucleon mass and the Greek letter μ to refer to a particle having a meson mass; M_1 is the mass of the incident projectile particle, M_2 is the mass of the target particle, M_3 is the mass of the spectator particle, and μ represents the created meson. In this paper we are concerned with the particular reaction

$$p + p \rightarrow n + p + \pi^+$$

at an incident proton momentum of 2.5 BeV/c; however, a description will be given for the more general case where the target and projectile particles are dissimilar.

Figure 2 is a schematic drawing of such a reaction where the following notation will be used:

q = four-momentum,

$\vec{q}$ = three-momentum,

w = total energy,

T = kinetic energy,

θ = polar angle measured relative to the direction of the incident particle of mass M_1,

and ϕ = azimuthal angle measured relative to the plane defined by $\vec{q}_{1L} \times \vec{q}_{3L}$.

Normally, when one of these variables is used it will be specified with two subscripts, the first identifying the particle, the second the reference frame. For example, $\vec{q}_{1L}$ signifies the three-momentum vector of the incident particle of mass M_1 in the laboratory frame. The second subscript is superfluous for a four momentum and will not be used; hence, the magnitude of a three momentum, for example q_{1L}, cannot be confused with the corresponding four momentum, q_1. Since the subscript 1 can refer to either the initial or the final-state particle of mass M_1, a prime (') will be used to designate the final-state particle in cases where confusion may arise.

It will be useful later to consider this reaction as composed of a two-particle final state in which one of the two particles immediately decays into two other particles. In Fig. 2 it has been pictured in this way. The interaction is seen as producing a particle of mass M_3 and a particle of mass M_Σ; M_Σ immediately decays into the observed particles $M_{1'}$ and M_μ. Since M_Σ can be treated as a variable this approach places no restrictions on our reaction.

2. P^2, W^2 Variables

We will choose the metric such that the four-dimensional scalar product

$$q \cdot q = -M^2$$

is in conformity with the notation of Chew and Low.[3] With this metric the variable Δ^2, defined as the invariant square of the difference of four momenta for the target (M_2) and the spectator (M_3) will be

$$\Delta^2 = (q_2 - q_3)^2 = 2 M_2 T_{3L} - (M_2 - M_3)^2 .$$

meson contained in the target particle. If we consider our reaction from the barycentric frame of the two nonspectator particles (M_1 and M_μ), in analogy with an elastic scattering process, we can define a polar scattering angle of particle M_1, θ_1^*, by

$$\cos(\theta_1^*) = \hat{q}_{1b} \cdot \hat{q}_{1b'},$$

where the subscript b connotes quantities in the center-of-mass system of the two final-state nonspectator particles. The direction of the projectile particle before and after scattering from the virtual meson defines a scattering plane whose normal is given by

$$\hat{n}_s = \hat{q}_{1b} \times \hat{q}_{1'b} .$$

A second plane can be defined by the directions of the target and spectator particles. This plane contains the direction of the virtual meson; its normal can be written as

$$\hat{n}_p = \hat{q}_{2b} \times \hat{q}_{3b} .$$

Again, in analogy with an elastic scattering process, we can define an azimuthal angle ϕ_1^* ranging from 0 to 360 deg by

$$\cos(\phi_1^*) = \hat{n}_p \cdot \hat{n}_s$$

in conjunction with the cross product of the same vectors to determine the quadrant of ϕ^*.

The parameter θ_1^* has relevance in that a differential cross section may be measured at a fixed value of W^2 and θ_1^* as a function of P^2. This differential cross section may be extrapolated similarly to the total cross section in order to obtain the differential cross section for the scattering of real particles of mass M_1 on real particles of mass μ at the fixed value of W^2 and θ_1^*. Thus, the entire process of extrapolation to obtain the total cross section for the process

$$M_1 + \mu \rightarrow M_1 + \mu$$

can also be applied to the differential cross section.[3]

The significance of ϕ_1^* was pointed out by Treiman and Yang[18] and can be illustrated with the help of Fig. 1. Since the only connection between the two previously defined planes $\hat{n}_s$ and $\hat{n}_p$ is through the dashed line representing the exchanged meson, and since this meson is assumed spinless, no correlation can exist between these planes; hence, the measured distribution can have no ϕ_1^* dependence.

4. Explicit Calculation of Scattering Angles

a. Invariant method. The scattering angel ϕ_1^* can be easily calculated by a method described by Chew and Low.[3] One considers the invariant

$$q_1 \cdot q_{1'}$$

first evaluated in the laboratory frame, where

$$q_1 \cdot q_{1'} = -w_{1L}\, w_{1'L} + q_{1L}\, q_{1'L} \cos(\theta_{1L}),$$

and then evaluated in the center-of-mass frame of the two nonspectator particles

$$q_1 \quad q_{1'} = -w_{1b}\, w_{1'b} + q_{1b}\, q_{1'L} \cos(\theta_1^*).$$

This scalar product must be the same in both systems and since the laboratory quantities can be measured and the center-of-mass quantities calculated from them, we can write an expression for $\cos(\theta_1^*)$ in terms of measurable or calculatable quantities:

$$\cos(\theta_1^*) = \frac{q_{1L}\, q_{1'L} \cos(\theta_{1b}) + w_{1'b}\, w_{1b} - w_{1'L}\, w_{1L}}{q_{1'b}\, q_{1b}}.$$

b. Direct transformation. The procedure used in this experiment to calculate $\cos(\theta_1^*)$ and ϕ_1^* was to explicitly transform the laboratory momentum vectors into the center-of-mass system of the two nonspectator particles and then to compute the center-of-mass scattering angles from their definitions as given in Sec. 2 of this appendix. Referring to Fig. 2, we can express our laboratory momentum vectors in a cartesian coordinate system oriented such that

$$\hat{q}_{1L} = \hat{Z} ,$$

$$\hat{q}_{1L} \times \hat{q}_{3L} = \hat{Y} ,$$

and as usual:

$$\hat{X} \times \hat{Y} = \hat{Z} .$$

The composite particle of mass M_Σ (= W) would then have a momentum vector $\vec{q}_{\Sigma L}$ which would lie in the same plane as $\vec{q}_{1L}$ and $\vec{q}_{3L}$. The transformation of a momentum vector in the laboratory frame into the center-of-mass frame of the two nonspectator particles to directly give the desired scattering angles can now be done in three steps. First the laboratory momentum vector is transformed to a coordinate system rotated by an angle $\theta_{\Sigma L}$. In this new frame a Lorentz transformation along the Z direction alone can transform our vector into the barycentric system of the nonspectator. Finally, a second rotation is performed to express the momentum vector relative to the direction of the projectile as seen in this frame. Thus, the entire transformation on a laboratory four vector can be written as

$$\begin{pmatrix} q_x \\ q_y \\ q_z \\ iw \end{pmatrix}_b = R(\alpha)\, L(\gamma)\, R(\theta_L) \begin{pmatrix} q_x \\ q_y \\ q_z \\ iw \end{pmatrix}_L ,$$

where $R(\theta)$ is the rotation matrix which generates a rotation about the Y axis by an angle θ. The matrix is given by[19]

$$R(\theta) = \begin{bmatrix} \cos(\theta) & 0 & \sin(\theta) & 0 \\ 0 & 1 & 0 & 0 \\ -\sin(\theta) & 0 & \cos(\theta) & 0 \\ 0 & 0 & 0 & 1 \end{bmatrix}.$$

The Lorentz transformation matrix $L(\gamma)$ along the Z axis is given by[20]

$$L(\gamma) = \begin{bmatrix} 1 & 0 & 0 & 0 \\ 0 & 1 & 0 & 0 \\ 0 & 0 & \gamma & -i\beta\gamma \\ 0 & 0 & i\beta\gamma & \gamma \end{bmatrix},$$

where

$$\gamma = \frac{w_{\Sigma L}}{M_\Sigma} \quad \text{and} \quad \beta = \sqrt{1 - \frac{1}{\gamma^2}} .$$

Since we are transforming from a frame where the M_Σ particle is moving to a frame where it is at rest, β must enter the Lorentz matrix (as we have written it) with a negative sign. M_Σ is identical with the square root of the previously defined variable W^2 and $w_{\Sigma L}$ can be calculated from energy conservation:

$$w_{\Sigma L} = w_{1L} + M_2 - w_{3L} .$$

The angle $\theta_{\Sigma L}$, because of momentum conservation, satisfies the relations

$$q_{3L} \sin(\theta_{3L}) = q_{\Sigma L} \sin(\theta_{\Sigma L})$$

and

$$q_{3L} \cos(\theta_{3L}) + q_{\Sigma L} \cos(\theta_{\Sigma L}) = q_{1L} .$$

These equations can be solved for $\cos(\theta_{\Sigma L})$ to give

$$\cos(\theta_{\Sigma L}) = \frac{q_{1L} - q_{3L}\cos(\theta_{3L})}{\sqrt{w_{\Sigma L}^2 - M_\Sigma^2}} .$$

The second rotation angle α signifies that specific rotation which is necessary to bring the projectile momentum vector in the center-of-mass frame of the two nonspectators parallel to the Z axis in that frame. More explicitly we have

$$\cos(\alpha) = \hat{q}_{1c} \cdot \hat{q}_{\Sigma L} ,$$

where

$$\begin{bmatrix} \vec{q}_1 \\ iw_1 \end{bmatrix}_c = L(\gamma)\, R(\theta_{\Sigma L}) \begin{bmatrix} \vec{q}_1 \\ iw_1 \end{bmatrix}_L .$$

Since all three successive transformations are in the plane defined by

$$\hat{n}_p = \hat{q}_{2L} \times \hat{q}_{3L} ,$$

the direction of the plane's normal will remain unchanged:

$$\hat{n}_p = \hat{q}_{2b} \times \hat{q}_{3b} .$$

This transformed momentum vector when expressed spherical coordinates will be in terms of the desired θ^* and ϕ^* variables. By referring to the definitions of the azimuthal angle ϕ^* of the previous section, we see that the only transformation needed to determine ϕ^* after the parameters $\phi_{\Sigma L}$, γ, and α have been determined, is on the nonspectator momenta since $\hat{n}_p$ is unchanged in the transformation. We can now write the scattering angles from the cartesian

representation by the usual formulas

$$\cos(\theta_1^*) = \frac{q_{1bz}}{q_{1b}},$$

$$\cos(\phi_1^*) = \frac{q_{1bx}}{\sqrt{q_{1bx}^2 + q_{iby}^2}},$$

and

$$\sin(\phi_1^*) = \frac{q_{1by}}{\sqrt{q_{1bx}^2 + q_{1by}^2}},$$

where the additional subscripts, x, y, and z refer to the cartesian components.

Finally, it is worth noting that for our particular reaction at 2.5 BeV/c, $\theta_{\Sigma L}$ will be a positive angle less than 90 deg. The second rotation angle α will be negative and also less than 90 deg in magnitude.

B. Calibration of Neutron Detectors

Because low energy neutrons can be detected in plastic scintillation material only indirectly through their interaction products, we can only detect either the charged particles that result from inelastic collisions with carbon nuclei or that result from elastic collisions involving the carbon or hydrogen nuclei which compose the scintillator. Both of these processes produce charged particles that have a spectrum of energies and that, for a fixed energy incident neutron, result in a continuous range of pulse heights from the photomultiplier. To limit ourselves to pulse heights which are significantly larger than most noise pulses, we biased the neutron counters so that they would be sensitive only to particles which would deposit in them an amount of light greater than that deposited by protons of approximately 4 MeV. Since at this energy most of the neutron interactions are elastic NP scatterings from the hydrogen in the scintillator, the lowest energy detectable neutron would also be 4 MeV.

Each of the 84 neutron counters was coupled to a tunnel diode discriminator.[15] The level of the discriminator -- in conjunction with the voltage on the phototube -- determined the bias for the counter. To bias for protons of approximately 4 MeV, we demanded that each counter be able to detect approx 20% of the 1.28 MeV γ rays from a Na^{22} source. This source was used to calibrate all the neutron counters and to ensure that no significant changes in sensitivity occurred during the Bevatron data run or during the later calibration run on the Lawrence Radiation Laboratory's 184 inch cyclotron.

Uncertainties in neutron timing that tended to increase the widths of the time bins came from two sources. The most significant was because the phototubes were required to operate with a very limited number of photons, which reflected itself in a time jitter of the resultant pulse, which in turn resulted in an uncertainty in the neutron time-of-flight determination. Secondly, since both the liquid hydrogen target and the neutron counters had a finite thickness, interactions in different parts of the target and detector gave rise to a difference of flight time for a given energy neutron.

To calibrate the apparatus and evaluate these uncertainties, timing measurements were made with neutrons of known energies. Since a detailed description has been published,[14] only a brief sketch and the results will be given here. The Lawrence Radiation Laboratory's 186 inch cyclotron was used to accelerate deutrons to approximately 450 MeV. They impinged on an internal target, producing a neutron beam of approximately one-half of their energy in the forward direction. A bending magnet cleared the resulting neutron beam of any charged particles and this beam was then allowed to strike a liquid hydrogen target. A counter range telescope was set to count the recoil protons from the elastic neutron-proton scatterings at a given angle and range of the protons. This defined a neutron beam of fixed energy and angle since only simple two-body kinematics in involved. Note that the energy spread of the initial neutron beam is irrelevant. The Chronotron and scintillation counter under calibration were set up to intercept this scattered neutron beam; hence, a direct calibration was possible since a trigger in the proton range telescope indicated that a neutron of known energy had struck the scintillation counter. The efficiency of each time bin for a particular neutron energy was defined as the total number of counts in the time bin divided by the total number of protons counted by the range telescope. By varying the angle of the proton telescope arm as well as the absorber thickness, one could measure the efficiency of each time bin as a function of neutron energy. Figure 9 shows the measured neutron detection efficiency for each of the seven time bins as a function of neutron energy. The mean energy and rms width as well as the mean P^2/μ^2 and corresponding rms width for the seven time bins are given in Table III.

C. A Survey of Positive Pion-Proton Elastic Scattering Angular Distributions

A compilation was made of data concerning angular distributions of elastically scattered positive pions on protons up to an incident pion kinetic energies of 525 MeV. The differential cross section at a particular energy was assumed to have the form

$$\frac{d\sigma}{d\Omega} = \lambda^2 \left[A + B\cos(\theta^*) + C\cos^2(\theta^*)\right],$$

where θ^* is the pion center of mass scattering angle and

$$\lambda = \frac{\hbar}{P_{cm}},$$

P_{cm} being the center-of-mass momentum of either particle.

For values of $P_{cm} < 140$ MeV/c (corresponding to laboratory pion energies less than 80 MeV), the coefficients, A, B, and C, can be well represented in terms of three phase shifts, α_3, α_{31}, and α_{33}, given by[32]

$$A = \sin^2 \alpha_3 + \sin^2(\alpha_{33} - \alpha_{31}),$$

$$B = 2\sin \alpha_3 \left[2\sin \alpha_{33} \cos(\alpha_{33} - \alpha_3) + \sin \alpha_{31} \cos(\alpha_{31} - \alpha_3)\right],$$

and

$$C = 3\left[\sin^2 \alpha_{33} + 2\sin \alpha_{31} \cos(\alpha_{33} - \alpha_{31})\right].$$

In this energy range, the momentum dependence of the phase shifts is fairly well known and is given by:[33]

$$\alpha_{33} = (0.234 \pm 0.019)\, P_{cm}^3,$$

$$\alpha_3 = (-0.110 \pm 0.004)\, P_{cm},$$

and

$$\alpha_{31} = (-0.044 \pm 0.005)\, P_{cm}^3,$$

where P_{cm} is measured in units of μc and the phase shifts are given in radians.

For $P_{cm} > 140$ MeV/c, a least squares fit of the coefficients A, B, and C, to the angular distributions at each momentum was used. They are plotted in Fig. 19. The momentum dependence of each coefficient was approximated by a smooth curve and incorporated into an IBM 7090 computer code called PIPRO. For $P_{cm} < 140$ MeV/c, the phase shifts were coded into PIPRO and used to determine the coefficients. In Fig. 19 is plotted the PIPRO approximation to these coefficients.

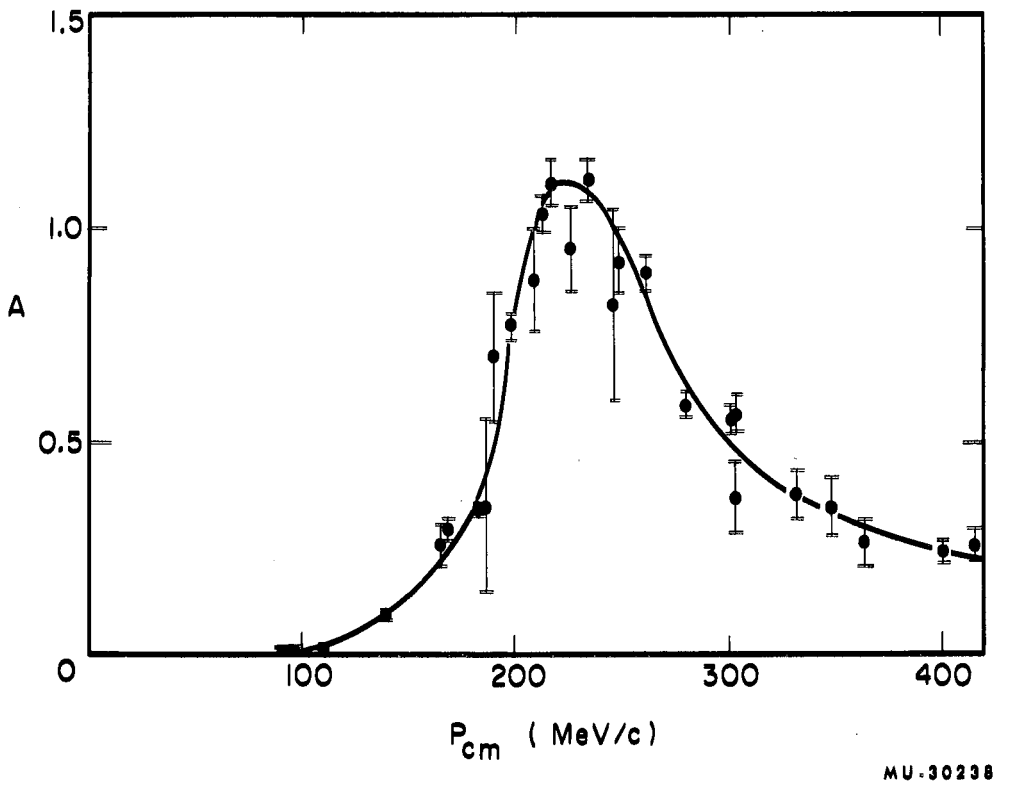

Fig. 19a. Angular distribution coefficient A as a function of center-of-mass momentum.

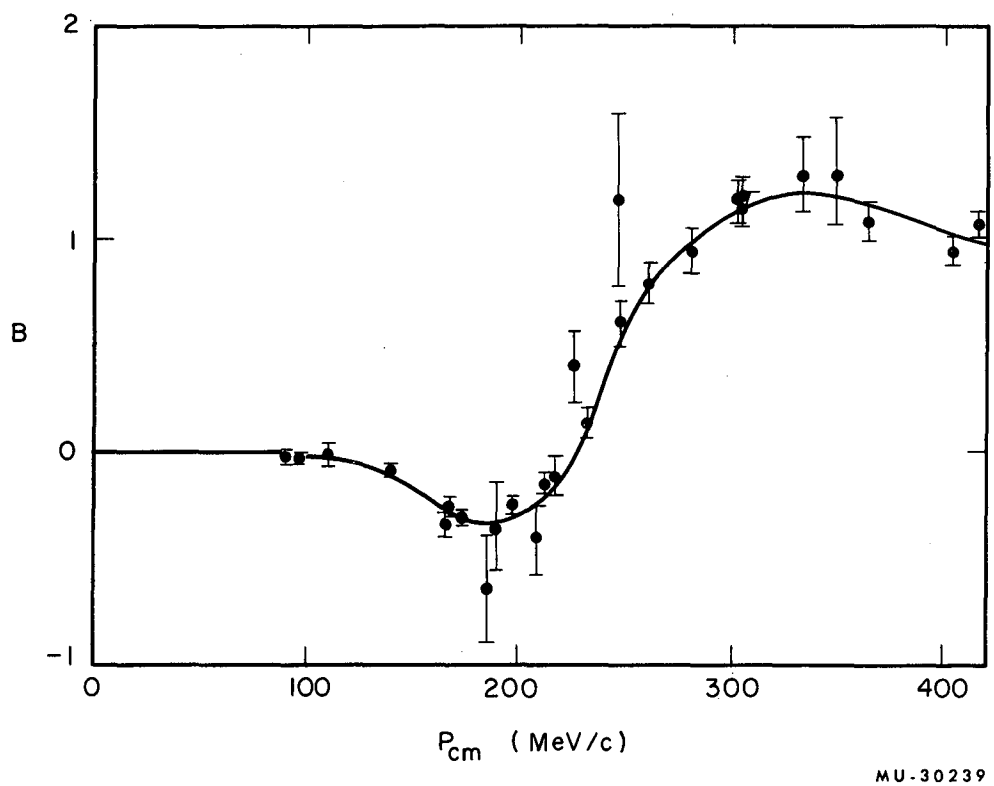

Fig. 19b. Angular distribution coefficient B as a function of center-of-mass momentum.

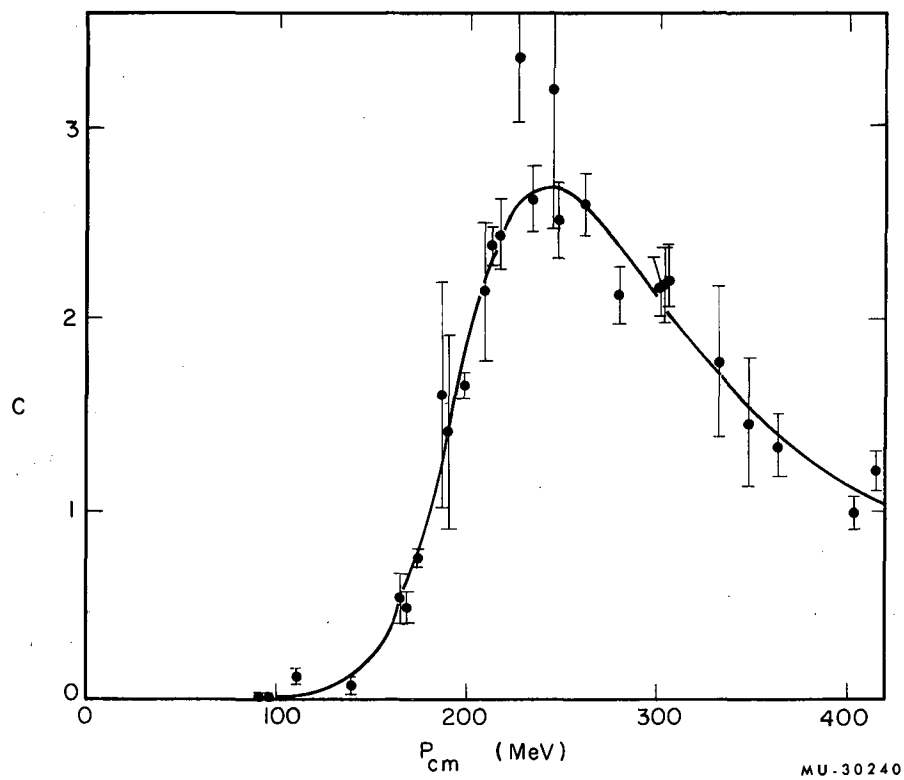

Fig. 19c. Angular distribution coefficient C as a function of center-of-mass momentum.

Footnotes and References

1. Yukawa, Proc. Physico-Math. Soc. Japan 17, 48 (1935).
2. G. F. Chew and F. E. Low, Phys. Rev. 101, 1570 (1956).
3. G. F. Chew and F. E. Low, Phys. Rev. 113, 1640 (1959).
4. W. B. Johnson, Study of $\pi^- + p \rightarrow \pi^+ + \pi^- + n$ at 1.25 and 1.75 BeV/c for Low Nucleon-Momentum-Transfer Collisions: Evidence for Pion-Pion Interactions (Ph. D. Thesis), Lawrence Radiation Laboratory Report UCRL-10703, February 27, 1963 (unpublished).
5. L. B. Auerbach, Study of Pion-Pion Scattering from the Reaction $\pi^+ + p \rightarrow \pi^+ + \pi^+ + n$ at 1.25 and 1.75 BeV/c (Ph. D. Thesis), Lawrence Radiation Laboratory Report UCRL-10530, October 31, 1962 (unpublished).
6. W. H. Barkas and A. H. Rosenfeld, Data For Elementary-Particle Physics, Lawrence Radiation Laboratory Report UCRL-8030 (Rev.), October 1, 1961 (unpublished), p. 8.
7. J. Orear, A. H. Rosenfeld, and R. Schluter, Nuclear Physics, Revised Edition (The University of Chicago Press, Chicago, Illinois, 1950), p. 49.
8. S. C. Baker, Q. A. Kerns, F. A. Kirsten, D. A. Mack, and T. A. Nunamaker, Nucl. Instr. Meth. 12, 1 (1961).
9. S. C. Baker, F. A. Kirsten, D. A. Mack, and C. Wiegand, Nucl. Instr. Meth. 12, 11 (1961).
10. S. C. Baker, Nucl. Instr. Meth. 12, 20 (1961).
11. A. E. Bjerke, Q. A. Kerns, and T. A. Nunamaker, Nucl. Instr. Meth. 12, 25 (1961).
12. Q. A. Kerns and G. C. Cox, Nucl. Instr. Meth. 12, 32 (1961).
13. F. Evans and F. A. Kirsten, Nucl. Instr. Meth. 12, 39 (1961).
14. C. E. Wiegand, T. Elioff, W. B. Johnson, L. B. Auerbach, J. Lach, and T. Ypsilantis, Rev. Sci. Instr. 33, 526 (1962).
15. A. E. Bjerke, Q. A. Kerns, T. A. Nunamaker, Pulse Shaping and Standardization of Photomultiplier Signals for Optimum Timing Information Using Tunnel Diodes, Lawrence Radiation Laboratory Report UCRL-9838, August 1961 (unpublished).

16. E. R. Cohen, K. M. Crowe, J. W. M. Dumond, The Fundamental Constants of Physics (Interscience Publishers, Inc., New York, 1957), p. 267.

17. R. Courant, Differential and Integral Calculus, Vol. 1 (Interscience Publishers, Inc., New York, 1937), p. 479.

18. S. B. Treiman and C. N. Yang, Phys. Rev. Letters 8, 140 (1962).

19. Herbert Goldstein, Classical Mechanics (Addison-Wesley Press, Inc., Cambridge, Mass, 1951), Ch. 4.

20. L. Landau and E. Lifshitz, The Classical Theory of Fields, (Addison-Wesley Press, Inc., Cambridge, Mass., 1951), Ch. 2.

21. Fortran Assembly Program (FAP) For the IBM709/7090 (International Business Machines Corporation, Data Processing Division, 112 East Post Road, White Plains, New York, 1961).

22. Reference Manual 709/7090 FORTRAN Programming System (International Business Machines Corporation, Data Processing Division, 112 East Post Road, White Plains, New York, 1961).

23. O. Chamberlain, Ann. Rev. Nucl. Sci. 10, 161 (1960).

24. Reference Manual Random Number Generation and Testing (International Business Machines Corporation, Data Processing Division, 112 East Post Road, White Plains, New York, 1959).

25. G5LC RANF Random Number Generator (Livermore), the standard random number generator used by the computing group of the Lawrence Radiation Laboratory, was checked for correlation of successive pairs of random numbers and none found. However, strong correlations between successive pairs were found if the generator was first run till a number less than 0.1 was produced and the correlation between the next two successive numbers examined. The power residue generators built into DRYLAB showed no such correlations. When RANF was inserted into DRYLAB, again five independent versions were used and none were ever called successively in the hope of minimizing the effect of this correlation. As mentioned in the main text, DRYLAB gave the same results whichever generator was used if coded in this way.

26. F. Selleri, Phys. Rev. Letters 6, 64 (1961). As written in his paper Eq. (I-3) has a factor of two missing. The corrected formula is used in our work.

27. G. B. Chadwick, G. B. Collins, P. J. Duke, T. Fujii, N. C. Hien, M. A. R. Kemp, and F. Turkot, Phys. Rev. 128, 1823 (1962).

28. G. A. Smith, H. Courant, E. C. Fowler, H. Kraybill, J. Sandweiss, and H. Taft, Phys. Rev. 123, 2160 (1961).

29. W. J. Fickinger, E. Pickup, D. K. Robinson, and E. O. Salant, Phys. Rev. 125, 2082 (1962).

30. The author thanks Professor G. F. Chew for a number of discussions on the applicability of this factor of two, and Professor Horace Taft, Dr. Gerald Smith, and Dr. W. J. Fickinger for confirming that their analysis was indeed done in this way.

31. W. J. Fickinger, E. Pickup, D. K. Robinson, and E. O. Salant, Phys. Rev. Letters 7, 196 (1961). Professor Horace Taft, in a priviate communication, feels this data is better fitted by an angular distribution of the form $1 + \cos^2(\theta^*)$. If this is so, then our data should have been multiplied by a factor of 2.5 rather than 3 for the comparison of Fig. 18.

32. A. I. Mukhin, E. B. Ozerov, B. M. Pontecorvo, E. L. Grigoriev, and N. A. Mitin, CERN Symposium, 214 (1956).

33. J. Ashkin, Supplement Nuovo Cimento, Vol. XIV, Series X, 221 (1959).

LEGAL NOTICE

This report was prepared as an account of Government sponsored work. Neither the United States, nor the Commission, nor any person acting on behalf of the Commission:

A. Makes any warranty or representation, expressed or implied, with respect to the accuracy, completeness, or usefulness of the information contained in this report, or that the use of any information, apparatus, method, or process disclosed in this report may not infringe privately owned rights; or

B. Assumes any liabilities with respect to the use of, or for damages resulting from the use of any information, apparatus, method or process disclosed in this report.

As used in the above, "person acting on behalf of the Commission" includes any employee or contractor of the commission, or employee of such contractor, to the extent that such employee or contractor of the Commission, or employee of such contractor prepares, disseminates, or provides access to, any information pursuant to his employment or contract with the Commission, or his employment with such contractor.